



## Seed bubbles stabilize flow and heat transfer in parallel microchannels

Jinliang Xu\*, Guohua Liu, Wei Zhang, Qian Li, Bin Wang

Micro Energy System Laboratory, Guangzhou Institute of Energy Conversion, Chinese Academy of Science, Guangzhou 510640, PR China

### ARTICLE INFO

#### Article history:

Received 2 December 2008

Received in revised form 2 March 2009

Accepted 13 March 2009

Available online 25 March 2009

#### Keywords:

Seed bubble

Microchannel

Boiling

Flow instability

Saturation seed bubble frequency

### ABSTRACT

Seed bubbles are generated on microheaters located at the microchannel upstream and driven by a pulse voltage signal, to improve flow and heat transfer performance in microchannels. The present study investigates how seed bubbles stabilize flow and heat transfer in micro-boiling systems. For the forced convection flow, when heat flux at the wall surface is continuously increased, flow instability is self-sustained in microchannels with large oscillation amplitudes and long periods. Introduction of seed bubbles in time sequence improves flow and heat transfer performance significantly. Low frequency ( $\sim 10$  Hz) seed bubbles not only decrease oscillation amplitudes of pressure drops, fluid inlet and outlet temperatures and heating surface temperatures, but also shorten oscillation cycle periods. High frequency ( $\sim 100$  Hz or high) seed bubbles completely suppress the flow instability and the heat transfer system displays stable parameters of pressure drops, fluid inlet and outlet temperatures and heating surface temperatures. Flow visualizations show that a quasi-stable boundary interface from spheric bubble to elongated bubble is maintained in a very narrow distance range at any time. The seed bubble technique almost does not increase the pressure drop across microsystems, which is thoroughly different from those reported in the literature. The higher the seed bubble frequency, the more decreased heating surface temperatures are. A saturation seed bubble frequency of 1000–2000 Hz can be reached, at which heat transfer enhancement attains the maximum degree, inferring a complete thermal equilibrium of vapor and liquid phases in microchannels. Benefits of the seed bubble technique are the stabilization of flow and heat transfer, decreasing heating surface temperatures and improving temperature uniformity of the heating surface.

© 2009 Elsevier Ltd. All rights reserved.

### 1. Introduction

Two-phase flow instabilities have been studied since 1950s. They may happen in power generation and heat transfer systems. Because of thermal management in small size systems, microfluidics plays an important role. Typical process must be considered when the channel hydraulic diameter becomes very small (Tadrist, 2007).

Two-phase flow instabilities consist of both static and dynamic ones (Xu et al., 2005a; Thome, 2006). The static flow instability can be characterized based on the demand curve of pressure drop against mass flux. Onset of flow instability (OFI) is identified as the minimum point of the demand curve. A lower flow rate than that at OFI condition leads to a flow rate excursion between single-phase liquid flow and two-phase flow. For the forced boiling flow in large size channels, it is recognized that three typical types of oscillations may occur: pressure drop type oscillation, density wave oscillation and thermal oscillation.

Flow instabilities in microchannels not only cause an uneven thermal stress on the heating surface, but also lead to an early

appearance of critical heat flux (CHF). Thus it is a notable problem if not addressed properly (Kuo and Peles, 2008). Recent studies worldwide on this topic focuses on either understanding of the flow instability mechanism, or mitigation means to suppress the flow instability. It is found that several experimental works evidenced these instabilities meanwhile only very limited theoretical developments exist in the literature (Tadrist, 2007).

Qu and Mudawar (2004) investigated transport phenomena in two-phase microchannel heat sinks. They identified two types of flow instabilities. Pressure drop oscillation was associated with periodic, large amplitude oscillations of inlet and outlet pressures and heat sink temperatures. Similar to pressure drop type instability in macrochannels, pressure drop instability in microchannels can be mitigated by setting a throttle valve at the upstream of microchannel heat sink. The parallel channel instability produces mild pressure and temperature oscillations.

Wu et al. (2006) performed visualizations and parameter measurements in an 8-microchannel heat sink, having a length of 60 mm and a hydraulic diameter of  $72.7 \mu\text{m}$  with a trapezoid cross-section. Two types of flow instabilities were identified. One is the liquid/two-phase alternative flow (LTAF) and the other is the liquid/two-phase/vapor alternative flow (LTVAF). The authors noted that the flow reversal of vapor core is the reason to produce

\* Corresponding author. Fax: +86 20 87057656.

E-mail address: [xujl@ms.giec.ac.cn](mailto:xujl@ms.giec.ac.cn) (J. Xu).

the alternative flow. The appearance of flow reversal in parallel microchannels is not in phase for different channels due to the flow or nucleation non-uniformity.

Hetsroni et al. (2006) performed studies of boiling heat transfer in parallel microchannels. Water and ethanol were used as the working fluids. Tests were performed in the range of hydraulic diameter of 100–220  $\mu\text{m}$ , mass flux of 32–200  $\text{kg}/\text{m}^2\text{s}$ , heat flux of 120–270  $\text{kW}/\text{m}^2$  and vapor mass quality of  $x = 0.01\text{--}0.08$ . The period between successive events depends on the boiling number and decreases with an increase in boiling number. Temporal variations of pressure drop, fluid and heating surface temperatures are periodic. Oscillation frequency is same for these parameters. All these fluctuations are in phase.

Kandlikar et al. (2006) noted that the flow boiling process suffers from severe instabilities due to nucleation of vapor bubbles

in a superheated liquid environment in a minichannel or microchannel. In an effort to improve the flow boiling stability, several modifications were introduced and experiments were performed in  $1054 \times 197 \mu\text{m}$  parallel rectangular microchannels (hydraulic diameter of 332  $\mu\text{m}$ ) with water as the working fluid. Effects of an inlet pressure restrictor and fabricated nucleation sites on the channel wall surfaces were evaluated as a means of stabilizing the flow boiling process and avoiding the backflow phenomenon. Results were compared with the unrestricted flow configurations in smooth channels.

Muwanga et al. (2007) studied flow boiling oscillation characteristics in two silicon microchannel heat sink configurations. One is the standard parallel heat sink consisting of 45 straight channels and the other is similar except with cross-linked paths at three locations. Both configurations show the decreased

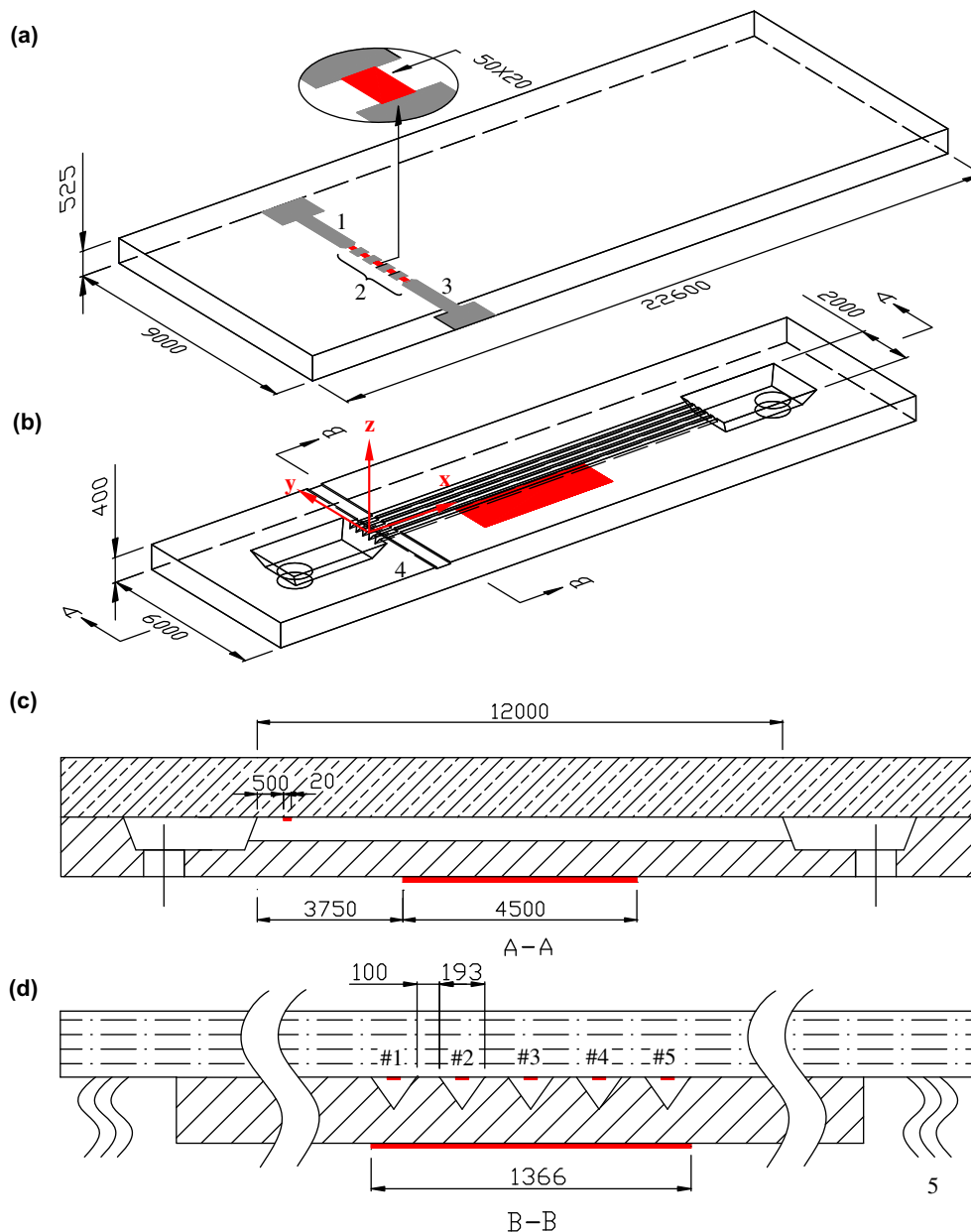


**Fig. 1.** Seed bubble guided heat transfer system, all dimensions are in  $\mu\text{m}$ , 1 and 3 are the resistances of gold pads ( $R_{Au1}$  and  $R_{Au2}$ ), 2 is the resistance of the five microheaters ( $R_h$ ), 4 is the bonding channel with the depth of 1.5  $\mu\text{m}$  to suspend the gold pad, 5 is the signal wire for the seed bubble generations, the red rectangular area in (b) is the effective heating area at the back surface of the silicon substrate.

oscillation frequencies with increases in heat fluxes. Oscillation properties were correlated for the standard straight microchannel heat sink.

Chang and Pan (2007) presented experimental results with a 15 parallel microchannel heat sink. Flow boiling demonstrates significantly different two-phase flow patterns under stable and unstable conditions. For the stable cases bubble nucleation, slug flow and slug or annular flow appear sequentially in the flow direction. On the other hand, forward or reversed slug/annular flows appear alternatively in each channel. A very narrow region for stable two-phase flow or mild two-phase flow oscillations is present near the zero exit vapor mass quality.

Huh et al. (2007) studied flow pattern transition instability during flow boiling in a single microchannel. A polydimethylsiloxane (PDMS) rectangular microchannel had a hydraulic diameter of 103.5  $\mu\text{m}$  and a length of 40 mm. Fluid pressures, inlet and outlet fluid temperatures and heating surface temperatures are found to be oscillating, matching the alternating flow pattern transitions versus time in the microchannel.

Lee and Pan (2008) investigated boiling heat transfer of water in a shallow microchannel with a uniform and a diverging cross-section.

Both microchannels had a depth of 20  $\mu\text{m}$  and a hydraulic diameter of 33.3  $\mu\text{m}$ . They found that performance of flow and heat transfer is improved in the diverging channel than those in the uniform one, primarily due to more stable two-phase flow in the diverging microchannel.

Wang et al. (2008) studied effects of inlet and outlet configurations on flow boiling instability in parallel microchannels, having a hydraulic diameter of 186  $\mu\text{m}$  and a length of 30 mm. Three types of inlet/outlet configurations were used. The type A configuration was restricted because the inlet and outlet conduits were perpendicular to the microchannels. The type B had no restrictions and the type C had inlet restrictions only. It is found that flow instability is strong for the type A configuration (conventional microchannel heat sink). While nearly stable flow and heat transfer status can be attained for the type C configuration with inlet fluid restriction. The performance of type B is in between those of the type A and C configurations. Therefore they recommended the type C configuration to mitigate flow instabilities during boiling flow in microchannels.

Thinking about the alternating flow instability in microchannels reported in the literature, the key issue is the strong thermal

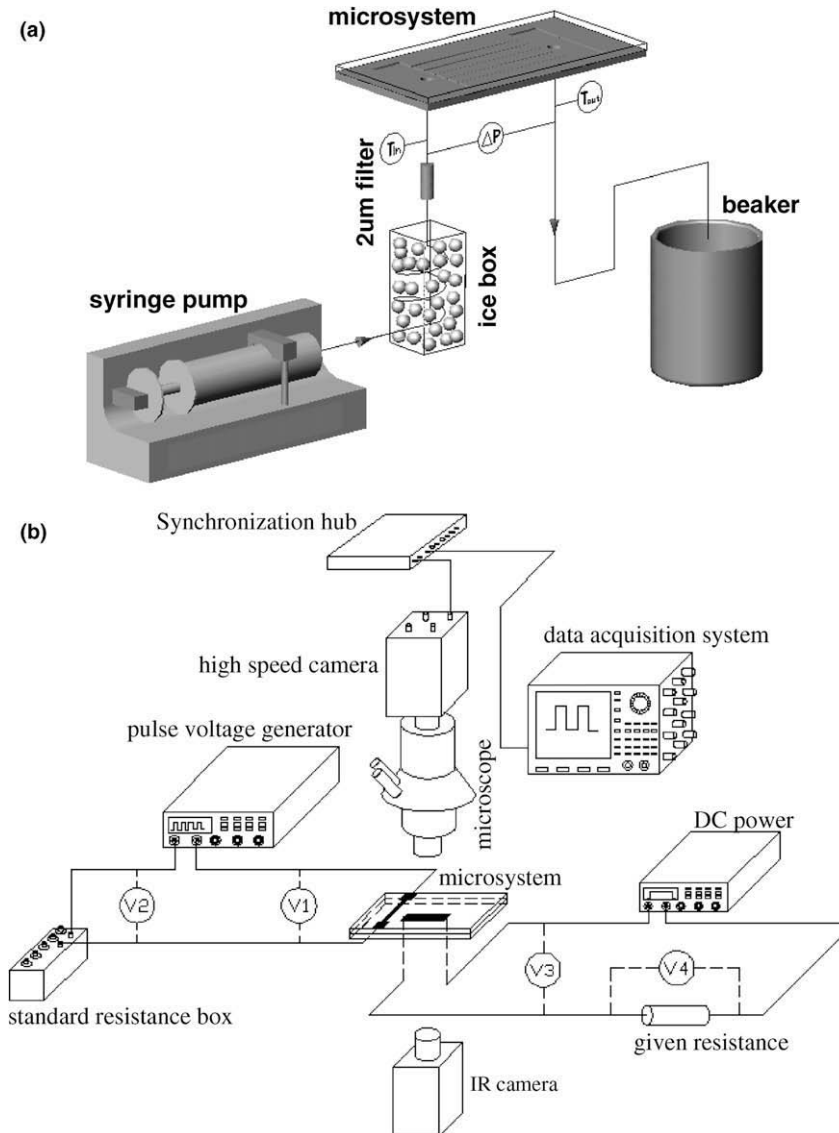


Fig. 2. (a) Forced convection loop and (b) measurement systems.

non-equilibrium of liquid and vapor phases in microchannels. This is true especially for the smooth silicon microchannels. Depending on different microfabrication techniques (dry or wet etching, etc.) used, roughness of channel walls may be varied from case to case. But it should be in nanometer. Lin (1998) reported a polysilicon surface to have a roughness of 6.5 nm, approaching the homogeneous bubble nucleation size for water. Boiling incipience needs very high temperature. High shear stress at the wall surface and less non-condensable gas in liquid also increase bubble nucleation temperatures. A detailed theoretical analysis of bubble nucleation in microchannels can be found in Li and Cheng (2004).

Considering liquid flow in microchannels if heating power is continuously increased, bubble nucleation does not appear until heating surface temperature and bulk liquid temperature are significantly superheated. Once boiling is triggered, the superheated liquid releases its stored energy to vapor phase through the nucleated bubble interface during a short time. A sharp pressure increase in the vapor core causes the fluid traveling in both downstream and upstream directions. The vapor growth and related pressure rise stage is complete when the superheated liquid completely releases its stored energy. It is noted that an external pumping pressure is always applied on the fluid, causing the subcooled liquid to refill the microchannels. It needs a long waiting time for the incoming liquid to reach the superheated bubble nucleation temperature again. The above processes are repeated in time sequence, causing the alternating flow pattern transitions in microchannels.

In the present paper, a new idea was proposed to mitigate flow instabilities in microchannels. Seed bubbles are generated at the

upstream of microchannels. The thermal non-equilibrium of vapor and liquid phases is well controlled by seed bubbles. Low frequency seed bubbles decrease oscillation amplitudes of various parameters. High frequency seed bubbles completely suppress flow instabilities. Using this technique, the uniformity of heating surface temperatures is improved. Significant heat transfer enhancement is also observed.

## 2. Experiment

### 2.1. Design of the seed bubble guided heat transfer system

Seed bubbles are generated on a group of microheater surfaces driven by a pulse voltage signal. They are swept away from microheaters when the pulse voltage signal is temporally off during a pulse cycle and flowing downstream along the liquid stream. Therefore, when liquid is superheated in microchannels, it releases its energy through the seed bubble interface on time, decreasing thermal non-equilibrium between liquid and vapor phases. Seed bubble frequency controls the thermal non-equilibrium degree. The higher the seed bubble frequency, the lower degree of thermal non-equilibrium between the two phases is. Because the incoming liquid from the microchannel entrance is subcooled, seed bubbles must have enough size thus they are not fully condensed before they contact the superheated liquid in microchannels. The recommended seed bubble size is  $\sim 10 \mu\text{m}$  for commonly used working fluids such as acetone in this study. Seed bubbles in this size range are not fully condensed in the microchannel upstream and will

**Table 1**  
Major physical properties of acetone at atmospheric pressure.

$T_{\text{sat}}$ (°C)	$\rho_f$ (kg/m <sup>3</sup> )	$C_{\text{pl}}$ (J/kg K)	$C_{\text{pg}}$ (J/kg K)	$h_{\text{fg}}$ (kJ/kg)	$\mu_f$ (Pa s)	$\mu_g$ (Pa s)	$k_f$ (W/m K)
56.3	748.0	2302.5	1380.6	512.94	$2.37 \times 10^{-4}$	$8.31 \times 10^{-6}$	0.518

Where  $T_{\text{sat}}$  is the saturation temperature,  $C_{\text{pl}}$  and  $C_{\text{pg}}$  are the specific heat of liquid and vapor,  $h_{\text{fg}}$  is the latent heat of evaporation,  $\mu_f$  and  $\mu_g$  are the viscosity of liquid and vapor,  $k_f$  is the thermal conductivity of liquid.

**Table 2**  
The parameter uncertainties or relative error.

Parameter	Explanation	Uncertainty or relative error
$Bo$	boiling number	7.0%
$f$	seed bubble frequency, Hz	0.001%
$G$	mass flux in microchannels, kg/m <sup>2</sup> s	1.2%
$L$ and $W$	length and width of each microheater, $\mu\text{m}$	0.1 $\mu\text{m}$
$L_{\text{film}}$ and $W_{\text{film}}$	length and width of the main heater, $\mu\text{m}$	0.1 $\mu\text{m}$
$m$	mass flow rate, kg/s	1.0%
$q$	heat flux at the main heater surface, W/m <sup>2</sup>	6.0%
$q_{\text{fi}}$	heat flux at the microheater surface, W/m <sup>2</sup>	5.0%
$q_{\text{side}}$	heat flux in terms of two side walls of triangular channels with the effective heating length of $L_{\text{film}}$ , W/m <sup>2</sup>	6.0%
$Q_{\text{ave}}$	time averaged electric energy consumed by the five microheaters, mW	6.0%
$R_{\text{Au1}}$ and $R_{\text{Au2}}$	two gold pad resistances, $\Omega$	1.0%
$R_f$	given resistance, $\Omega$	1.0%
$R_s$	resistance selected from the standard resistance box, $\Omega$	0.1%
$Re$	liquid Reynolds number	1.2%
$St_{\text{dev}}$	standard deviation of the heating surface temperature, °C	0.5 °C
$T_{\text{fi}}$	microheater temperature, °C	2 °C
$T_{\text{in}}$ and $T_{\text{out}}$	inlet and outlet fluid temperatures, °C	0.3 °C
$T_{\text{film,a}}$	average temperature at the main heater, °C	0.5 °C
$T_{\text{film,c}}$	temperature at the main heater centerline, °C	0.5 °C
$u_{\text{ave}}$	average liquid velocity at the microchannel entrance, m/s	1.0%
$V_1$ and $V_2$	voltages in the microheater circuit, see Fig. 2, V	0.1 mV
$V_3$ and $V_4$	Voltages in the main heater circuit, see Fig. 2, V	0.1 mV
$x$ and $y$	coordinate in the axial and width directions, see Fig. 1, m	0.1 $\mu\text{m}$
$x_{\text{film}}$ and $y_{\text{film}}$	attached coordinate on the main heater, see Fig. 1, m	0.1 $\mu\text{m}$
$\alpha$	heat transfer coefficient, W/m <sup>2</sup> K	7.0%
$\phi$	thermal efficiency	6.0%
$\Delta p$	pressure drop, Pa	0.1%

**Table 3**

Runs performed for the flow instability experiment.

Run	$G$ (kg/m <sup>2</sup> s)	$q$ (kW/m <sup>2</sup> )	$T_{in}$ (°C)	$T_{out}$ (°C)	$f$ (Hz)	$u_{ave}$ (m/s)	$Bo \times 1000$	$\tau_c$ (s)	$\delta_p$ (kPa)
1	377.9	439.4	5.9	52.8	*	0.51	2.27	26.30	4.10
2	377.9	439.1	6.0	52.8	10	0.51	2.27	14.73	2.10
3	377.9	440.1	6.2	52.6	100	0.51	2.27	*	*
4	377.9	439.9	2.2	52.9	1000	0.51	2.27	*	*
5	377.9	438.2	2.5	52.6	2000	0.51	2.26	*	*
6	377.9	452.8	2.9	52.6	*	0.51	2.34	25.20	4.70
7	377.9	453.2	3.0	52.9	10	0.51	2.34	18.30	2.81
8	377.9	453.2	3.3	52.9	100	0.51	2.34	*	*
9	377.9	452.5	3.6	52.5	1000	0.51	2.33	*	*
10	377.9	452.7	3.8	52.9	2000	0.51	2.34	*	*
11	377.9	467.0	4.8	52.4	*	0.51	2.41	39.82	6.27
12	377.9	468.0	4.8	53.0	10	0.51	2.41	13.42	3.07
13	377.9	468.6	5.0	53.3	100	0.51	2.42	*	*
14	377.9	468.4	4.9	53.0	1000	0.51	2.42	*	*
15	377.9	467.8	4.9	52.8	2000	0.51	2.41	*	*
16	377.9	484.0	5.2	53.1	*	0.51	2.50	26.67	6.24
17	377.9	484.0	5.4	53.2	10	0.51	2.50	13.43	3.36
18	377.9	484.4	5.4	53.3	100	0.51	2.50	*	*
19	377.9	484.5	5.5	53.3	1000	0.51	2.50	*	*
20	377.9	484.8	5.5	53.3	2000	0.51	2.50	*	*
21	598.4	601.5	3.4	50.1	*	0.80	1.96	45.21	6.30
22	598.4	600.7	4.4	52.6	10	0.80	1.96	15.27	4.32
23	598.4	602.1	3.5	49.7	100	0.80	1.95	*	*
24	598.4	602.9	4.3	52.6	1000	0.80	1.96	*	*
25	598.4	603.0	4.4	51.6	2000	0.80	1.96	*	*
26	598.4	625.5	4.6	52.8	*	0.80	2.04	14.52	7.92
27	598.4	626.3	4.7	53.1	10	0.80	2.04	8.21	4.03
28	598.4	627.1	4.9	53.4	100	0.80	2.04	*	*
29	598.4	627.2	5.1	52.9	1000	0.80	2.04	*	*
30	598.4	626.6	5.3	52.9	2000	0.80	2.03	*	*
31	598.4	649.0	3.0	51.7	*	0.80	2.11	27.51	8.86
32	598.4	649.7	3.4	52.3	10	0.80	2.12	11.72	4.71
33	598.4	650.0	3.2	52.3	100	0.80	2.11	*	*
34	598.4	652.2	3.0	52.5	1000	0.80	2.12	*	*
35	598.4	652.0	3.2	52.4	2000	0.80	2.12	*	*
36	598.4	688.0	4.1	52.9	*	0.80	2.24	16.36	9.49
37	598.4	688.6	4.2	53.2	10	0.80	2.24	8.13	5.12
38	598.4	688.9	4.5	53.4	100	0.80	2.24	*	*
39	598.4	689.9	4.8	53.4	1000	0.80	2.24	*	*
40	598.4	689.5	5.0	53.8	2000	0.80	2.24	*	*
41	598.4	723.4	4.2	53.5	*	0.80	2.36	12.73	8.62
42	598.4	724.5	4.2	53.9	10	0.80	2.36	7.23	5.23
43	598.4	724.1	4.2	53.6	100	0.80	2.36	*	*
44	598.4	724.9	4.3	53.6	1000	0.80	2.36	*	*
45	598.4	726.3	4.4	54.1	2000	0.80	2.37	*	*
46	755.9	848.4	3.9	54.2	*	1.01	2.19	23.30	9.42
47	755.9	850.0	4.0	54.1	10	1.01	2.19	6.58	6.25
48	755.9	857.9	4.6	54.2	100	1.01	2.21	*	*
49	755.9	851.0	4.6	54.2	1000	1.01	2.19	*	*
50	755.9	851.2	4.5	54.5	2000	1.01	2.19	*	*
51	897.6	936.4	2.1	50.7	*	1.20	2.03	23.34	10.98
52	897.6	936.2	2.3	52.2	10	1.20	2.03	8.89	8.87
53	897.6	937.4	2.3	52.6	100	1.20	2.04	*	*
54	897.6	936.9	2.4	53.0	1000	1.20	2.03	*	*

Note.  $\tau_c$  and  $\delta_p$  are the cycle period and oscillation amplitude of pressure drops, which are only given for the self-sustained oscillation flow and the seed bubble guided flow at  $f = 10$  Hz. The symbol \* in the sixth column represents the run without seed bubbles assisted. The symbol \* in the last two columns represents the stable flow with seed bubbles assisted.

evolve the heat transfer controlled growth once they contact the superheated liquid somewhere in microchannels.

Fig. 1 shows the seed bubble stabilized heat transfer system, consisting of a top 7740 glass cover (Fig. 1a) bonded with a bottom silicon substrate (Fig. 1b). The whole system had a length of 22.6 mm. The glass cover had a width of 9.0 mm, which was wider than the silicon substrate by 3.0 mm, leaving two 1.5 mm margins in the width direction to ensure the signal wire bonding for seed bubble generators. The glass cover and silicon substrate had a thickness of 525  $\mu\text{m}$  and 400  $\mu\text{m}$ , respectively. At the back surface of the glass cover, five platinum film microheaters were connected consecutively by a gold film, acting as the seed bubble generator array (see the red and black area in Fig. 1a). Each platinum film microheater had a size of 50  $\mu\text{m}$  by 20  $\mu\text{m}$ , facing the downward

triangular microchannel center. The microheater array was 500  $\mu\text{m}$  downstream following the microchannel entrance (see Fig. 1c).

In the silicon substrate, two conical cavities were etched and followed by two circular holes, acting as the inlet and outlet fluid pools. The two circular holes had a diameter of 1.0 mm and were connected with capillary tubes. Each microchannel had a width of 193.2  $\mu\text{m}$  and a depth of 136.6  $\mu\text{m}$  to form a hydraulic diameter of 100  $\mu\text{m}$ . The distance between two neighboring microchannels was 100  $\mu\text{m}$  in the width direction, forming a whole width of 1366  $\mu\text{m}$  for the microchannel area. The microchannels had a length of 12000  $\mu\text{m}$ . In order to ensure success bonding of the silicon wafer and glass cover, a bonding channel with a depth of 1.5  $\mu\text{m}$  was etched on the top surface of the silicon substrate.

The bonding channel was wider than the gold pad by  $10\ \mu\text{m}$ , thus the gold pad was suspended in the  $1.5\ \mu\text{m}$  channel. Packaging of the microsystem includes seal of the bonding channel by glue to prevent liquid leakage.

At the back surface of the silicon substrate, a platinum film heater with a length of  $4500\ \mu\text{m}$  and a width of  $1366\ \mu\text{m}$  was deposited centrally in both axial and width directions, acting as the heating source for the heat transfer system. Cross-sections of A–A and B–B referring to Fig. 1b are shown in Fig. 1c–d. Five microchannels were named as #1–5 in Fig. 1d.

A coordinate system was established, with  $x$ ,  $y$ , and  $z$  as the axial flow direction, chip width direction, and chip thickness direction, respectively (see Fig. 1b). The coordinate of  $(0,0,0)$  is at the microchannel entrance in axial direction, chip centerline in width direction and top surface of the silicon substrate. The flow was always from left to right, referring to Fig. 1. In order to evaluate heating surface temperatures at the back surface of the silicon chip ( $4500 \times 1366\ \mu\text{m}$ ), another two-dimensional attached coordinate system ( $x_{\text{film}}, y_{\text{film}}$ ) was set, with  $x_{\text{film}} = 0$  at the beginning of the effective heating area, and  $y_{\text{film}} = 0$  at the centerline of the heating area. Regarding the two coordinate systems, we have  $x = x_{\text{film}} + 3750$  in the unit of micron. Temperatures at the thin film heater (the red planar area in Fig. 1b) are measured by an infrared radiator imaging system.

The microsystem was fabricated by the standard MEMS (micro-electromechanicals) technique. The five triangular microchannels were etched with a depth of  $136.6\ \mu\text{m}$  by KOH. Back side titanium film and platinum film were deposited at the back surface of silicon wafer with a thickness of  $1000\ \text{\AA}$  and  $1500\ \text{\AA}$ , respectively. Initially a photoresist layer was spun on the  $7740$  glass surface. After patterning with the photolithography technique, a titanium layer of  $200\ \text{\AA}$  a platinum layer of  $1500\ \text{\AA}$  and a gold layer of  $3000\ \text{\AA}$  were sputtered successively on the glass surface. After the photolithograph process, the chemical etching technique was used to remove the gold film selectively, exposing the five platinum film heaters for the seed bubble generators. Finally the glass cover and silicon substrate were bonded together. The fabrication procedure of microchannels is similar to that used by

Wu and Cheng (2004). Thus the microchannel roughness should be less than  $10\ \text{nm}$ .

## 2.2. Parameter measurements

As shown in Fig. 2a, a syringe pump supplied pure acetone liquid to the microsystem. A  $2\ \mu\text{m}$  filter was arranged in the loop to prevent solid particles entering the microsystem. Soft capillary tubes connected each component of the loop together. Because acetone has a low saturation temperature of  $56.3\ ^\circ\text{C}$  at atmospheric pressure and the silicon wafer has a large axial thermal conduction effect, it is possible to initiate boiling process in the inlet fluid pool for very low mass flow rates. An ice box containing a copper capillary tube with flowing acetone liquid inside was arranged in the loop. Fine K-type thermocouples with a  $0.1\ \text{mm}$  diameter were installed as close to the microsystem as possible, to measure fluid temperatures ( $T_{\text{in}}, T_{\text{out}}$ ). A pressure drop transducer across the microsystem measured the pressure drop ( $\Delta p$ ). Outlet of the microsystem was at the atmospheric pressure. The produced vapor by the microsystem was fully condensed in the outlet capillary tube. The condensed liquid was collected by a glass beaker. The syringe pump gave the flow rate value directly. The microsystem was horizontally positioned. Before the experiment, liquid acetone was vigorously boiled in a glass container for 5 minutes to remove non-condensable gas. Then the liquid was cooled to the room temperature and charged in a glass cylinder arranged in the syringe pump for experimental use.

Fig. 2b shows the experimental setup not including the forced convection loop. An electric function generator sent pulse voltage signal to drive the microheater array for seed bubble generation. The pulse signal had output frequencies  $f$  from  $0.2$  to  $20\ \text{MHz}$  and voltage amplitudes from  $0$  to  $20\ \text{V}$ . A precision resistance box supplied a selective, precision resistance in the range from  $0.01$  to  $1000\ \Omega$ . The commonly used resistance is  $1\ \Omega$  in this study. Typical current flowing through the circuit was on the magnitude of  $100\ \text{mA}$ . Also due to the large size of the resistance box, temperature rise by the Joule heating effect can be neglected to maintain a constant resistance used. Current flowing through the circuit was

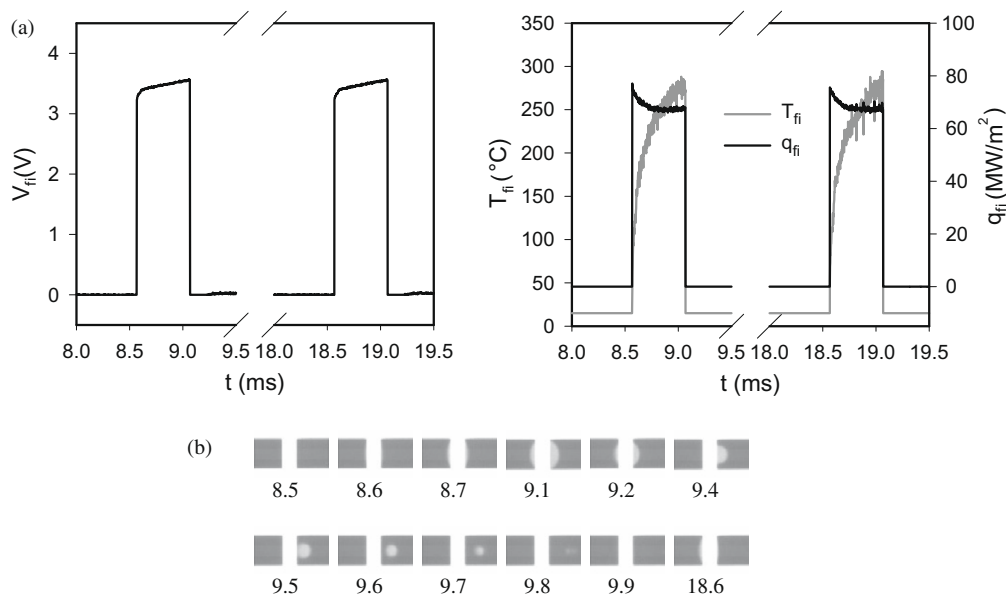


**Fig. 3.** (a) Voltage, temperature, and heat flux on the platinum film microheater array for seed bubble generation under flow condition, (b) periodic seed bubble generation and departure on the microheater 3 (time unit is ms),  $G = 377.9\ \text{kg}/\text{m}^2\text{s}$ ,  $q = 315.5\ \text{kW}/\text{m}^2$ ,  $Bo = 0.001626$ ,  $f = 100\ \text{Hz}$ , pulse cycle period  $\tau = 10\ \text{ms}$ , pulse duration time  $\tau_d = 0.5\ \text{ms}$ .

obtained by measuring the voltage  $V_2$  due to the known selected resistance. Voltage applied on the five microheaters was  $V_1$ . Both  $V_1$  and  $V_2$  were measured by a DL750 high speed data acquisition system.

A DC power supplier heated the thin film heater ( $4500 \times 1366 \mu\text{m}$ ), providing a constant heat flux boundary condition at the precisely selected area. In such a circuit, a given resistance of  $1 \Omega$  was included, across which the voltage was measured by  $V_4$ . The voltage applied on the heating area was  $V_3$ . Thus heating power on the heating area was computed as  $V_3 V_4 / R_f$ , where  $R_f$  is the given resistance.

Measurement instruments are indicated in Fig. 2b. A Leica MZ16 stereo-microscope (Germany) was bonded with a high speed camera (HG100K, USA). Two recording rates were used, 5000 frames per second for fast transient observations and 30 frames per second for slow flow pattern transitions. The microheater length of  $50 \mu\text{m}$  corresponds to 20 pixels in the visualization area.

Thus spatial resolution of the optical system was about  $2.5 \mu\text{m}$  per pixel.

At the back surface of the silicon substrate, the thin film heating area was measured by a high resolution, high accuracy infrared radiator imaging system (FLIR ThermoCAM SC3000IR). A micro optical lens was adapted in front of the IR image system, to increase the spatial resolution. The system has a thermal sensitivity of  $0.02 \text{ }^\circ\text{C}$  at  $30 \text{ }^\circ\text{C}$ , a spatial resolution of  $1.1 \text{ mrad}$ . A typical resolution of  $320 \times 240$  pixels over the focused heating area allowed for the precise determination of maximum temperature and temperature gradients over the whole heating area of  $4500 \mu\text{m}$  by  $1366 \mu\text{m}$ . The IR camera was centrally located so that the heating area of the silicon wafer was in the visualization area. The image system was connected to a central control computer (not shown in Fig. 2).

The IR temperature measurement required a careful calibration of the emissivity, depending on the surface topography and

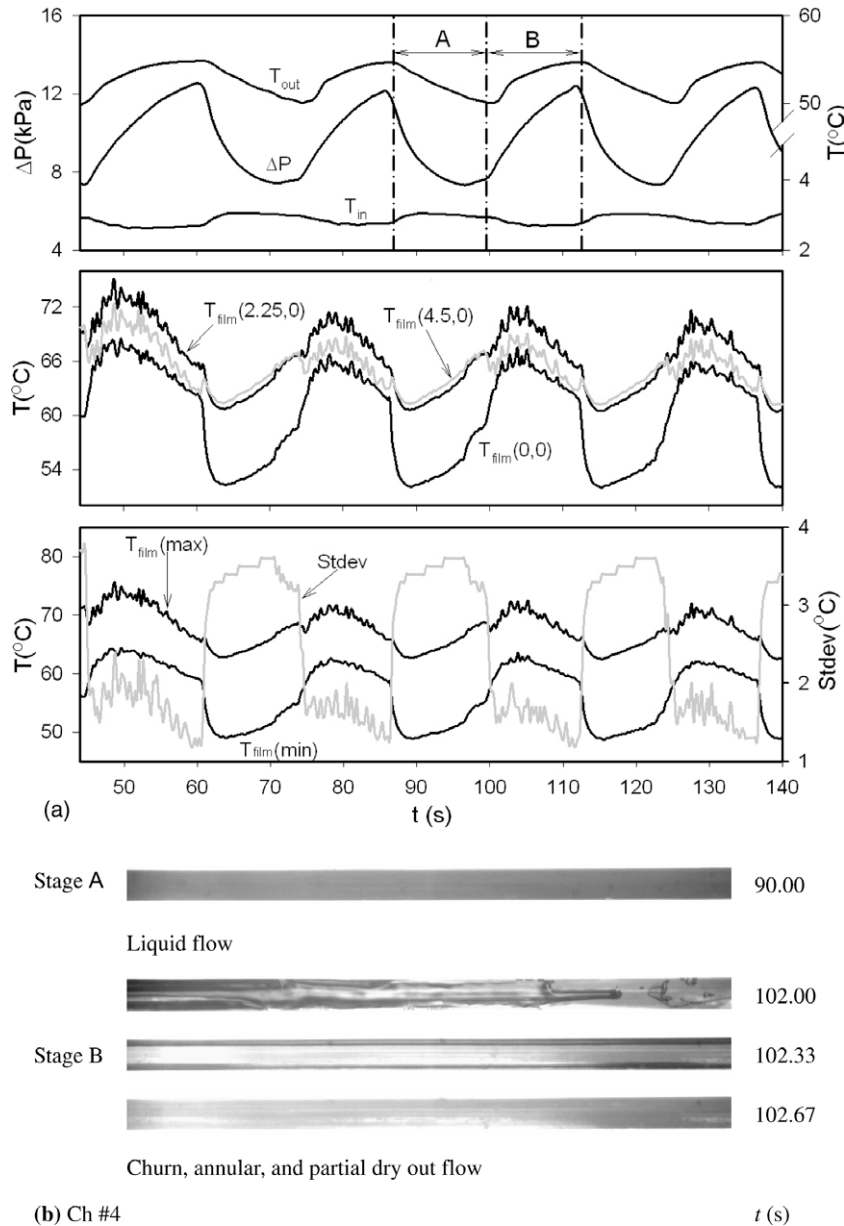


Fig. 4. (a) Parameter variations of the self-sustained flow instabilities with  $G = 377.9 \text{ kg/m}^2 \text{ s}$ ,  $q = 452.8 \text{ kW/m}^2$ ,  $Bo = 0.002335$ , (b) flow pattern transitions for the self-sustained flow instability.

wavelengths that are interrogated (Xu et al., 2005b). A very thin black lacquer was uniformly painted on the thin film surface of the silicon wafer. An emissivity of 0.94 yields good measurement accuracies. The temperature dependence of emissivity in the present experimental data range can be neglected. The IR imaging system was calibrated against a set of standard temperatures with an accuracy of 0.5 °C.

During the experiment, the high speed data acquisition system, the high speed camera and the IR imaging system were in the waiting mode. A synchronization hub sent a signal to trigger functions of these systems. The maximum time difference of the initial function of the three systems after they receive the triggering signal from the synchronization hub is smaller than 20 ns. A central control computer collected all image files and data from the measurement systems.

### 2.3. Data reduction

#### 2.3.1. Microheater temperature computations

As seen from Fig. 1a, the microheater array consisted of five platinum film resistance of  $R_{fi}$  and two gold pad resistances of  $R_{Au1}$  and  $R_{Au2}$ . At the room temperature,  $R_{Au1} = R_{Au2} = 0.902 \Omega$ . Calibration technique was performed to determine the electric resistance of microheaters with respect to temperatures. The whole microsystem was in an oven with precisely controlled temperatures having an uncertainty of 0.5 °C. A low DC voltage ( $\sim 100$  mV) supplied the microheater array, maximally lowering the microheater temperature rise due to Joule heating.  $V_1$  and  $V_2$

were measured by a data acquisition system instantaneously. Under the known resistances of  $R_{Au1}$ ,  $R_{Au2}$ , and  $R_s$  (the selected resistance from the resistance box, see Fig. 2b), the platinum film resistance was computed as  $R_{fi} = V_1 R_s / V_2 - R_{Au1} - R_{Au2}$ , relating to  $T_{fi}$  (microheater temperature). The calibration process attained a linear relation of microheater resistances with respect to temperatures as  $R_{fi} = 0.0434 T_{fi} + 25.33$ . The calibrated temperature range was from the room temperature to 120 °C. Extension of the correlation to higher temperatures than 120 °C led to an acceptable accuracy due to the good linear behavior. During the formal experiment for seed bubble generation, the electric circuit computation obtains the Joule heating power at the platinum film surfaces as

$$Q(t) = \left( \frac{V_2(t)}{R_s} \right)^2 \left( \frac{V_1(t)}{V_2(t)} R_s - R_{Au1} - R_{Au2} \right) \quad (1)$$

Average heat flux on the five platinum microheater surfaces is  $q_{fi}(t) = Q(t)/(NLW)$ , where  $N$  is the number of microheaters, same as that of microchannels,  $L$  and  $W$  are the microheater length and width, which are 50  $\mu\text{m}$  and 20  $\mu\text{m}$ , respectively.

#### 2.3.2. Data reductions for other parameters

The liquid used in this study is pure acetone ( $\text{CH}_3\text{COCH}_3$ , molecular weight of 58.08, purity larger than 99.5%). Acetone has a low saturation temperature of 56.3 °C at atmospheric pressure and is widely used as the working fluid in micro heat pipes and loop heat pipes. Other working fluids, such as FC-72, methanol and ethanol, can also be used for microscale heat transfer experiments. They have similar thermal physical properties. Water is a different

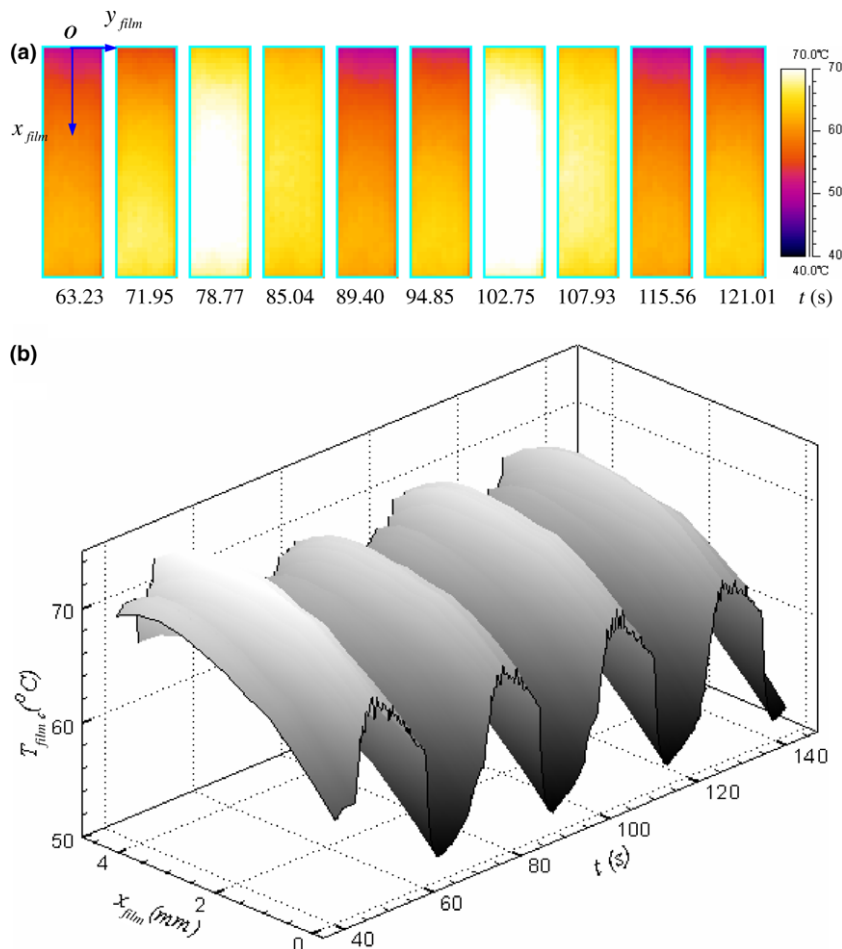


Fig. 5. Self-sustained oscillations of heating surface temperatures.

coolant in its high saturation temperature and large latent heat of evaporation. Thus it is not used in this study. The major physical properties are shown in Table 1, cited from Yaws (1999). The data reduction process involves determinations of mass flux  $G$ , heat flux  $q$ , boiling number  $Bo$  and liquid Reynolds number  $Re$ .

Mass flux  $G$  was defined as the total mass flow rate over the cross-sectional area of the five triangular microchannels,  $G = m / (NA_c)$ , where  $N$  is the number of microchannels, which was 5 in this study,  $A_c$  is the cross-sectional area of a single microchannel. The volume flow rate  $Q_v$  is directly from the reading of the syringe pump, mass flow rate is  $m = \rho_f Q_v$ , where  $\rho_f$  is the liquid density.

Heat flux  $q$  at the film heater area ( $4500 \times 1366 \mu\text{m}$ ) was computed as  $q = \varphi V_3 V_4 / (R_f L_{\text{film}} W_{\text{film}})$ , where  $\varphi$  is the thermal efficiency, which is the ratio of heat received by the fluid to the total heating power,  $R_f$  is the given resistance of  $1 \Omega$  in the DC power supplier

circuit,  $L_{\text{film}}$  and  $W_{\text{film}}$  are the length and width of the thin film heater.

Boiling number  $Bo$  is defined as  $Bo = q / (G h_{\text{fg}})$ , where  $h_{\text{fg}}$  is the latent heat of evaporation.

Liquid Reynolds number  $Re$  is defined as  $Re = u_{\text{ave}} d / \nu$ , where  $u_{\text{ave}}$  is the average liquid velocity in microchannels,  $d$  is the hydraulic diameter of microchannels ( $100 \mu\text{m}$  here), and  $\nu$  is the liquid kinematic viscosity based on the inlet liquid temperature.

In order to characterize temperature uniformity of the heating surface, the standard deviation was introduced. The average heating surface temperature was computed as

$$T_{\text{film,a}} = \frac{\sum_{i=1}^I \sum_{j=1}^J T_{ij}}{I \times J} \tag{2}$$

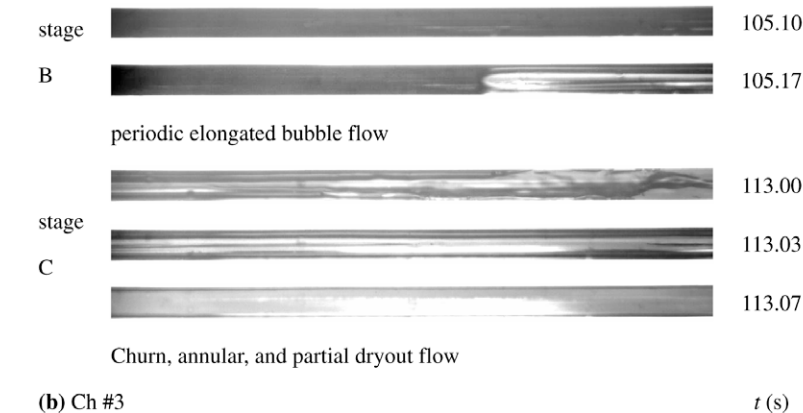
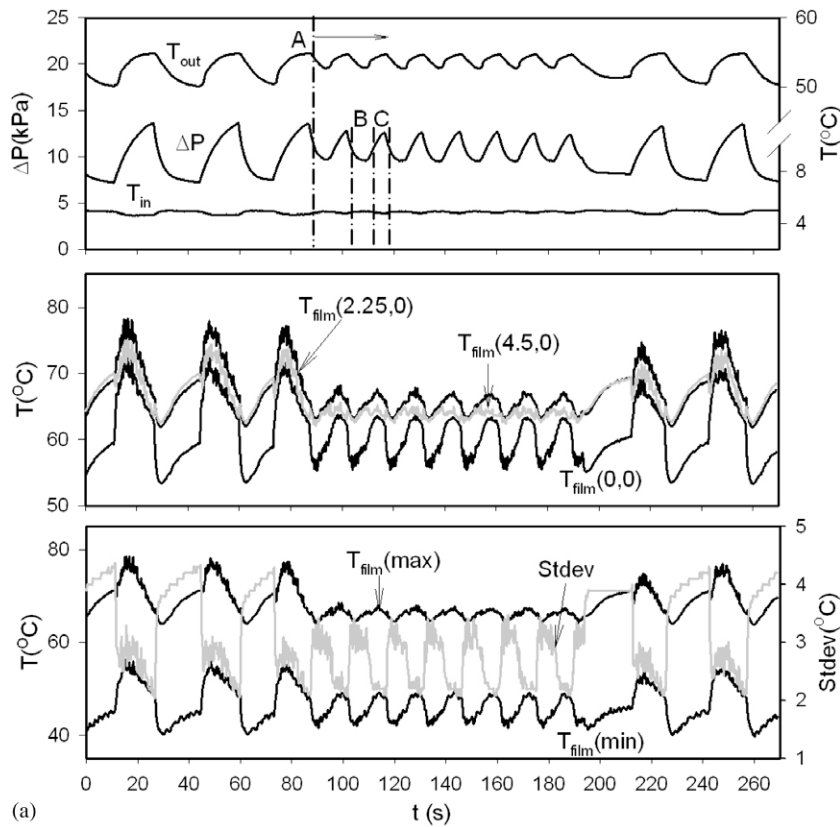


Fig. 6. (a) Parameter variations with (the central part,  $f = 10 \text{ Hz}$ ) and without seed bubbles assisted at  $G = 377.9 \text{ kg/m}^2 \text{ s}$ ,  $q = 467.0 \text{ kW/m}^2$ ,  $Bo = 0.00241$ . (b) Flow pattern transitions for the seed bubble guided flow at low frequency of  $10 \text{ Hz}$ .

where  $T_{ij}$  is the local temperature on the thin heating film at the location of  $(x_{\text{film}}, y_{\text{film}})$ ,  $I$  and  $J$  are the maximum grid numbers in  $x_{\text{film}}$  and  $y_{\text{film}}$  directions for temperatures in the heating area ( $4500 \times 1366 \mu\text{m}$ ). The Stdev number was computed as

$$\text{Stdev} = \sqrt{\frac{\sum_{i=1}^I \sum_{j=1}^J (T_{ij} - T_{\text{film,a}})^2}{I \times J}} \quad (3)$$

The Stdev number has the temperature unit of  $^{\circ}\text{C}$ . It should be zero for an absolutely uniform temperature distribution. The higher the Stdev number, the larger degree of non-uniformity of heating surface temperatures is.

The spatial-averaged heat transfer coefficient is computed as

$$\alpha = \frac{q_{\text{side}}}{T_{\text{film,a}} - T_f} \quad (4)$$

where  $q_{\text{side}}$  is the heat flux based on the heating area of two side walls of microchannels with the effective heating length of  $4500 \mu\text{m}$ ,  $T_f$  is the fluid temperature. It is noted that the heat transfer coefficient may be changed versus time for the oscillation flow.

#### 2.4. Uncertainty analysis

The pressure drop transducer has an accuracy of 0.1% with a response time of 0.1 s. Thermocouples have an accuracy of 0.3  $^{\circ}\text{C}$  with a response time of 0.1 s. Flow rate given by the syringe pump has an accuracy of 1.0%. The IR imaging system has a temperature uncertainty of 0.5  $^{\circ}\text{C}$  with a response time of 0.25 s. Performing the standard error analysis yields uncertainties of mass flux of 1.2% and liquid Reynolds number of 1.2%.

Many factors influence the effective thermal efficiency  $\phi$ . Heat loss of the microsystem includes components of radiation and natural convection heat transfer from the heated chip surface to environment. Heat loss also includes thermal conduction from the microsystem to its upstream and downstream connection tubes. It is quite difficult to estimate the heat flux uncertainty accurately. A set of single-phase liquid flow experiment was performed. The thermal efficiency  $\phi$  was decided with the heat received by acetone liquid (computed from mass flow rate and inlet/outlet fluid temperature differences) divided by the total applied heating power. The applied heating power is the major factor influencing the thermal efficiency. Generally, the higher the applied heating power, the larger the thermal efficiency is. The calibrations identified the highest thermal efficiency of 0.82 and the smallest value of 0.76. Thus we selected the average value of 0.79, under which the maximum uncertainty of  $\phi$  is 6.0%. Giving the fact that the voltage measurement is very accurate (the DL750 data acquisition system has an error of 0.1 mV for the voltage measurement), this estimation of  $\phi$  directly leads to the uncertainty of heat flux of 6.0%. The parameter uncertainties are summarized in Table 2.

### 3. Experimental procedure

The following experimental procedure was applied.

1. Setup a specific flow rate.
2. Leave the high speed data acquisition system, optical measurement system and IR imaging system in the waiting mode.
3. Apply and increase heating powers on the thin film heater ( $4500 \times 1366 \mu\text{m}$ ), until the maximum chip temperature begins to be larger than the saturation temperature of  $56.3 \text{ }^{\circ}\text{C}$  at atmospheric pressure.
4. Increase the heating power by a small step.
5. Leave the whole system operate steadily for half an hour.

6. Trigger the synchronization hub. Thus the high speed data acquisition system records all related parameters. The high speed camera records flow images in microchannels. The IR imaging system records heating surface temperatures. The recording time should be at least several seconds. The measurements are exactly synchronized.
7. Select suitable pulse voltage signal frequency  $f$  and voltage amplitude, trigger the pulse voltage signal.
8. Let the system sustains the seed bubble guided heat transfer mode for more than 100 seconds.
9. Turn off the pulse voltage signal and let the system returns to the previous flow and heat transfer state without seed bubbles. Note that all the measurement systems have been continuously collecting data and image files from step 6 to 9.
10. Such a run is complete.
11. Change the pulse voltage signal (the most important parameter is the pulse frequency), and repeat the above processes.
12. Change flow rate or heating power on the back heating surface, repeat the above process.

Table 3 shows the 54 runs performed in this paper. The data ranges are as follows: mass flux  $G$  of  $377\text{--}898 \text{ kg/m}^2 \text{ s}$ , heat flux  $q$  of  $439\text{--}936 \text{ kW/m}^2$ , seed bubble frequency  $f$  of  $10\text{--}2000 \text{ Hz}$ . The inlet liquid temperatures are generally low such as less than  $10 \text{ }^{\circ}\text{C}$ . For some runs, low seed bubble frequencies such as 1 and 5 Hz are tested but these runs are not listed in Table 3.

## 4. Results and discussion

#### 4.1. Seed bubble generation and departure

Considering microheaters immersed in flowing liquid, bubble growth is separated into an early isothermal growth stage controlled by large pressure difference across the bubble interface ( $p_v - p_f = 2\sigma R \sim 4.0 \times 10^4 \text{ Pa}$  when  $R$  is  $1 \mu\text{m}$ , where  $\sigma$  is the surface tension force,  $R$  is the bubble radius), and a subsequent isobaric growth. Onset of bubble nucleation temperature depends on microheater design, pulse heating parameters and working fluid. Seed bubble diameter  $\sim 10 \mu\text{m}$  is preferable, at which pressure difference across the bubble interface is not significant, and bubble growth is considered as heat transfer controlled. It is observed that seed bubbles in this size range are not fully condensed in microchannels thus they are effective for the improvement of flow and heat transfer in microchannels.

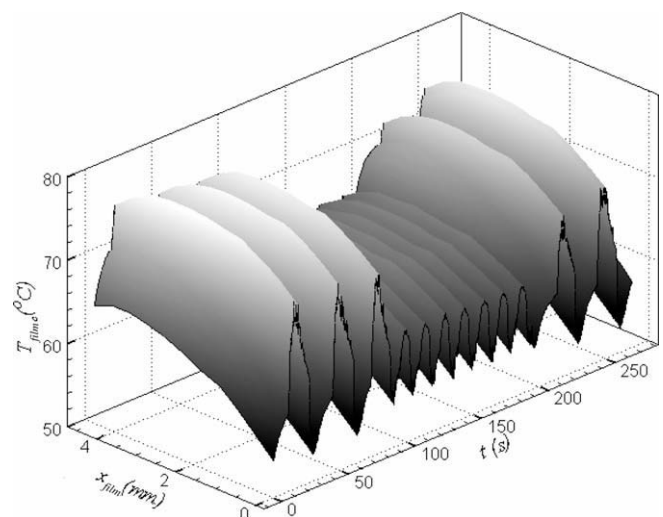


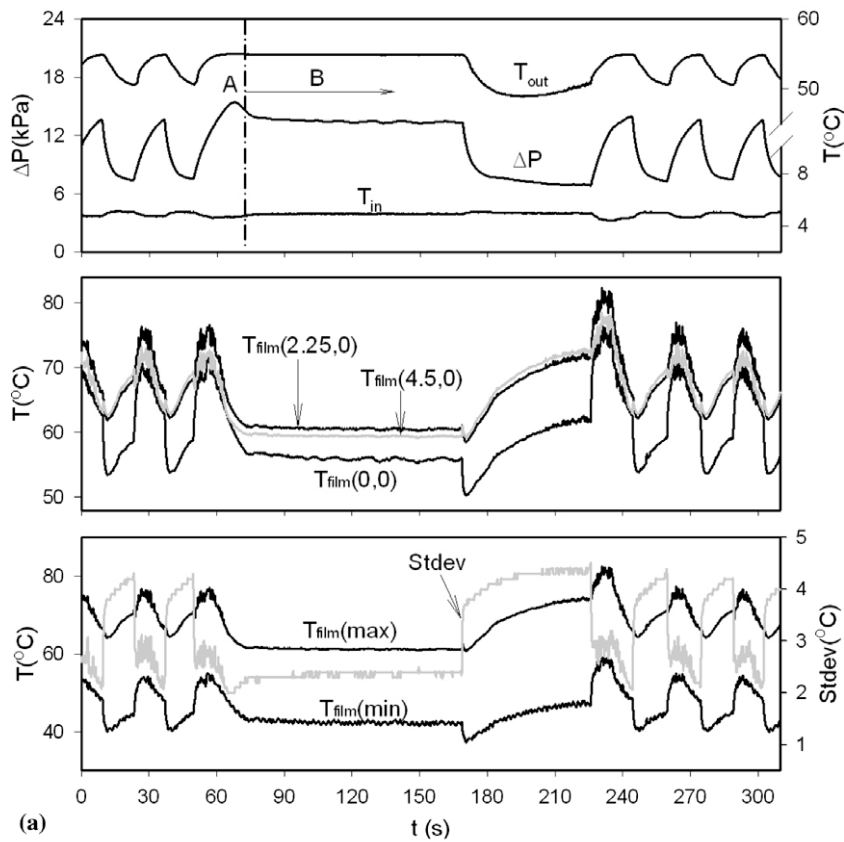
Fig. 7. Heating surface temperatures with ( $f = 10 \text{ Hz}$ ) and without seed bubbles assisted.

The capillary number,  $Ca = \mu_f u_{ave} / \sigma$ , is on the magnitude of  $10^{-3}$ , maintaining seed bubbles in spherical shape (Takahashi et al., 1999). When the pulse voltage signal is on during a pulse cycle, microheaters have higher surface temperatures than the surrounding solid and liquid, thus seed bubbles are on the microheater surfaces due to the Marangoni force drawing seed bubbles toward the higher temperature area of microheaters. Once the pulse voltage signal is off during the pulse cycle, microheaters recede to the liquid temperature quickly thus the Marangoni effect disappears. A shear force from the flowing liquid stream ( $4\pi\mu_f Ru_{ave} \sim 1$  mN), flushes seed bubbles away from microheaters. Consecutive pulses control the seed bubble generation and departure.

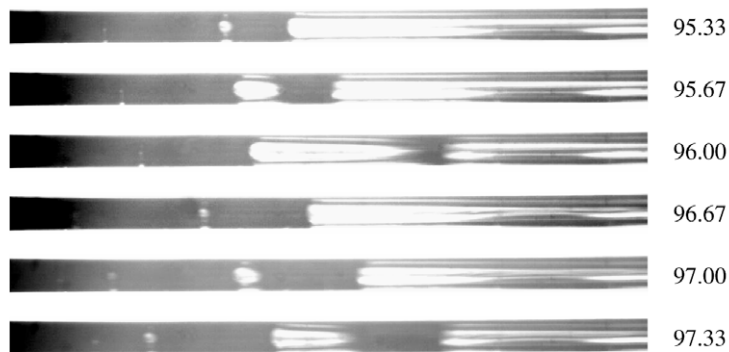
In this study, the pulse signal frequency  $f$  is from 10 to 2000 Hz. For each run of seed bubble generation, we increase the voltage applied on the microheater array, until miniature bubbles can be seen

through the microscope. An example run is given in Fig. 3 with  $f = 100$  Hz (pulse cycle period  $\tau = 10$  ms), pulse duration time  $\tau_d = 0.5$  ms. During the pulse duration time in each cycle, voltage ( $V_{fi}$ ) on the microheater array is increased slightly, but heat flux ( $q_{fi}$ ) is decreased slightly. Meanwhile microheater temperatures ( $T_{fi}$ ) are continuously increased (see Fig. 3a). Seed bubble generations are observed by the high speed camera referring to the channel #3 (see Fig. 3b). A seed bubble appears at about  $t = 8.7$  ms and continuously grows after that time. When the pulse signal is off at  $t = 9.2$  ms, the seed bubble leaves the microheater and flows downstream. When the second pulse signal comes, a new seed bubble appears at  $t = 18.6$  ms.

The time averaged electric energy consumed by the five microheaters,  $Q_{ave}$ , depends on the heat flux  $q_{fi}$ , the pulse duration time  $\tau_d$  and the pulse cycle period  $\tau$  ( $\tau = 1/f$ ), which is calculated as



(a)



Quasi-stable rear elongated bubble interface

(b) Ch #3

$t$  (ms)

**Fig. 8.** (a) Parameter variations with ( $f = 1000$  Hz) and without seed bubbles assisted,  $G = 377.9$  kg/m<sup>2</sup> s,  $q = 467.0$  kW/m<sup>2</sup>,  $Bo = 0.00241$ . (b) Flow patterns for the seed bubble guided flow at high frequency of  $f = 1000$  Hz.

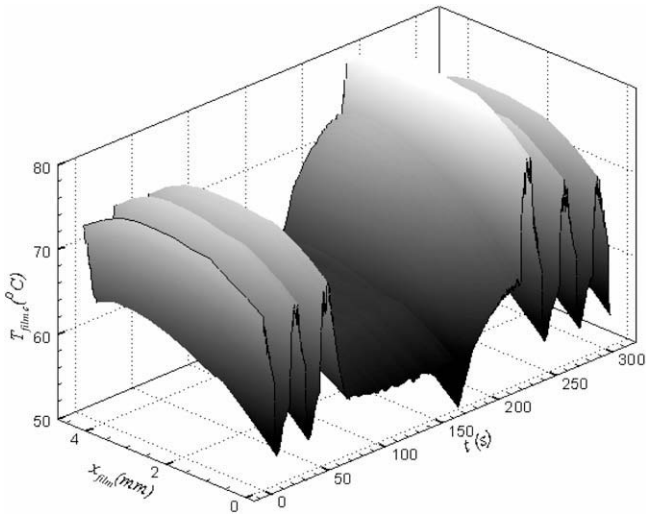


Fig. 9. Heating surface temperatures with ( $f = 1000$  Hz) and without seed bubbles assisted.

$$Q_{ave} = \frac{N \int_0^{\tau_d} q_{fi} LW dt}{\tau} = NLWf \int_0^{\tau_d} q_{fi} dt = f \int_0^{\tau_d} Q(t) dt \quad (5)$$

The calculation results give  $Q_{ave}$  as 0.35, 3.5, 17.5, 70 and 105 mW for  $f = 1, 10, 100, 1000$  and 2000 Hz, respectively. These values are very small compared with the heat load in the main heater. The liquid temperature rise in the seed bubble generation process is estimated to be 0.006, 0.06, 0.3, 1.2 and 1.8 °C for  $f = 1, 10, 100, 1000$  and 2000 Hz, respectively. It is neglectable for  $f < 100$  Hz but it has a couple of degrees for  $f = 1000$ –2000 Hz.

#### 4.2. Self-sustained flow instabilities in parallel microchannels

In the present data range, the flow is unstable without seed bubbles assisted. Fig. 4a shows oscillations of various parameters for  $G = 377.9$  kg/m<sup>2</sup> s,  $q = 452.8$  kW/m<sup>2</sup> and  $Bo = 0.002335$ . The oscillation cycle period is 25.6 s and the oscillation amplitude of pressure drop is 5.1 kPa. It is found that pressure drop ( $\Delta p$ ), outlet fluid temperature ( $T_{out}$ ) and heating surface temperatures ( $T_{film}$ ) are oscillating at the same cycle period. The inlet fluid temperature ( $T_{in}$ ) oscillates at small amplitude. Pressure drop and outlet fluid temperatures are nearly in phase. But pressure drop and inlet

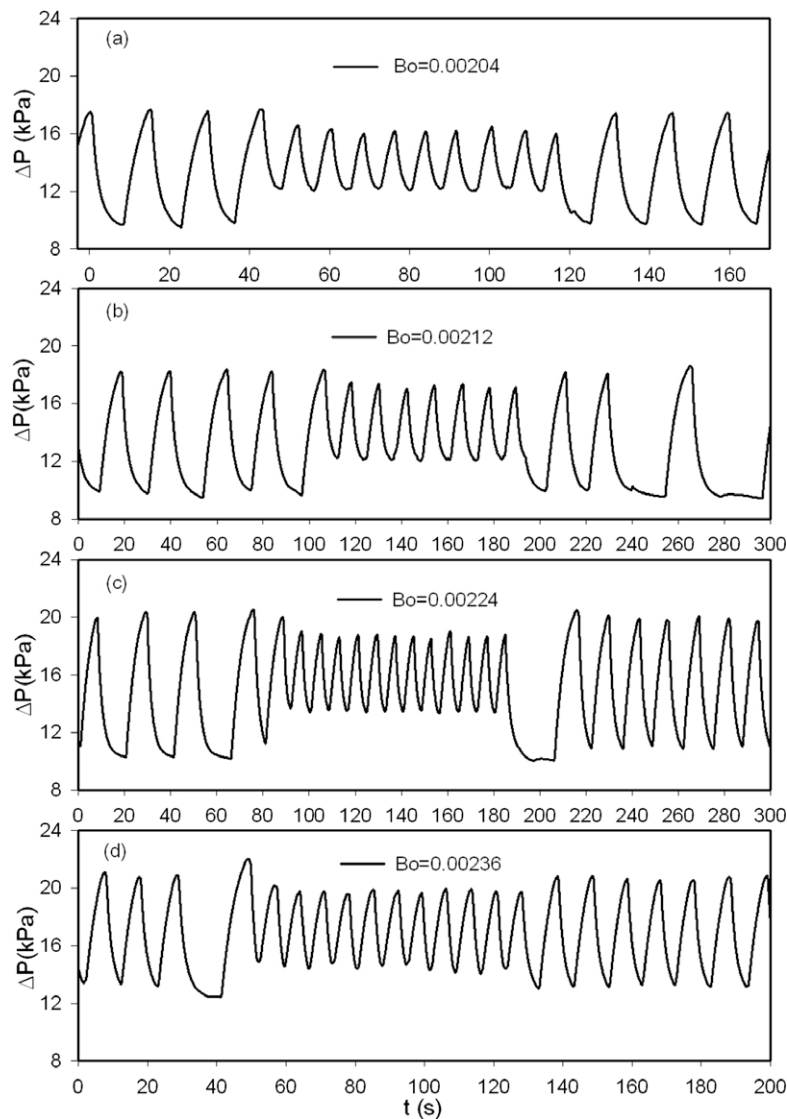


Fig. 10. Effect of boiling numbers on pressure drop oscillations with ( $f = 10$  Hz) and without seed bubbles assisted at  $G = 598.4$  kg/m<sup>2</sup> s.

liquid temperature are out of phase. During each oscillation cycle, heating surface temperatures attain the maximum value earlier than the pressure drop, indicating the phase shift between pressure drop and heating surface temperatures. The flow is a typical alternating one with long cycle period and large amplitude. Fluctuations of heating surface temperatures with small amplitude and short period (high frequency) are embedded in the long period/large amplitude oscillations, when the temperatures are higher in the long cycle, indicating the multiscale phenomenon. This phenomenon is related to the fast flow pattern transitions in the two-phase flow stage, which will be shown later. The Stdev numbers are out of phase with the heating surface temperatures. Low heating surface temperatures correspond to large Stdev number, indicating the large degree of non-uniformity of heating surface temperatures.

As shown in Fig. 4a, an oscillating cycle consists of a pressure drop decrease stage A and a pressure drop increase stage B. Heating surface temperature attains the maximum at  $t = 103$  s, and pressure drop attains the maximum at  $t = 112$  s, indicating the phase shift between the two parameters. Fig. 4b shows flow patterns with time synchronized to the heating surface temperatures in channel #4. Liquid flow appears at  $t = 90$  s in the stage A. The

churn, annular and partial dry-out flows appear at  $t = 102.00$  s,  $102.33$  s and  $102.67$  s in the stage B, respectively. These flow patterns are switched in the timescale of milliseconds, accounting for the short period/small amplitude oscillations of heating surface temperatures in the higher temperature period.

Fig. 5a shows heating surface temperatures on the heating area ( $4500 \times 1366 \mu\text{m}$ ). Fig. 5b shows heating surface temperatures at the centerline ( $y_{\text{film}}$ ) versus time. Oscillation amplitudes are larger at the heating surface upstream than those at other locations, attaining more than  $12^\circ\text{C}$ . Temperature difference in the chip width direction is generally small within  $1^\circ\text{C}$ . This is true for other cases.

4.3. Seed bubbles mitigate flow instabilities at low seed bubble frequencies

When the self-sustained oscillation flow appears in microchannels, introduction of seed bubbles in time sequence mitigates flow instabilities at low seed bubble frequencies such as  $f = 10$  Hz. The heat transfer system returns to the self-sustained oscillation flow if seed bubbles are turned off. An example run is shown in Fig. 6 for  $G = 377.9 \text{ kg/m}^2 \text{ s}$ ,  $q = 467.0 \text{ kW/m}^2$  and  $Bo = 0.00241$ . Seed

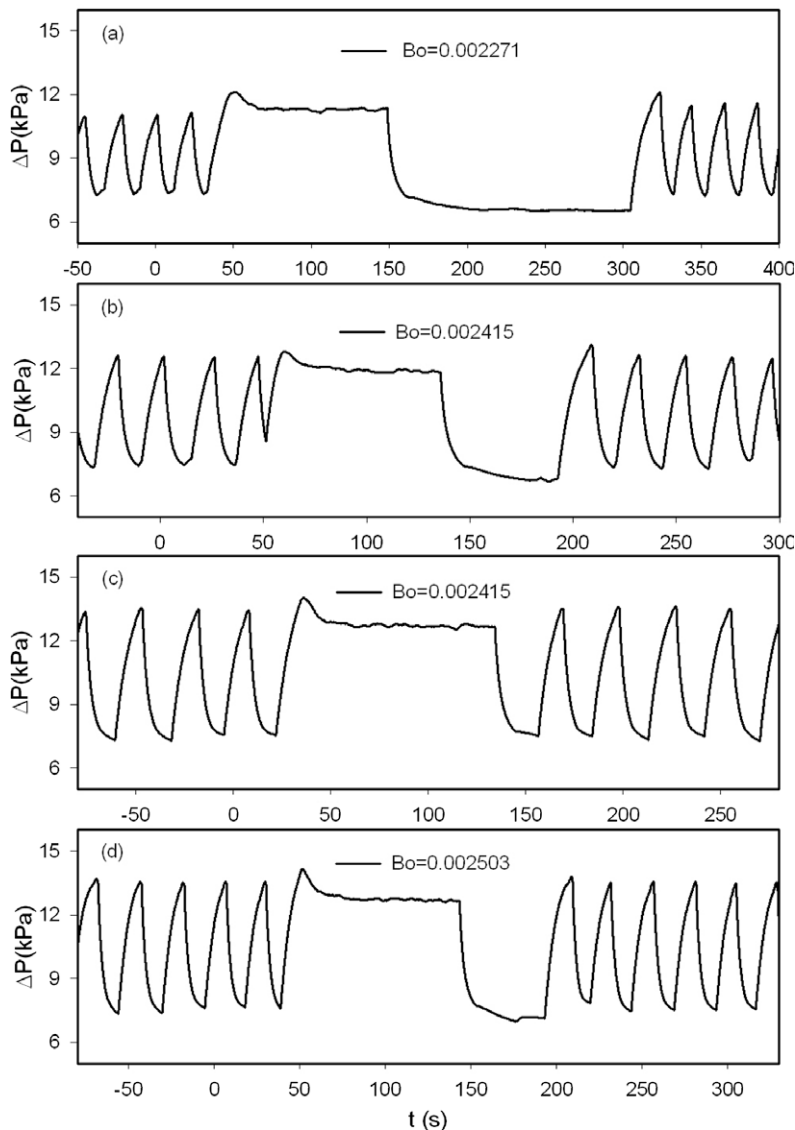


Fig. 11. Effect of boiling numbers on pressure drop signals with ( $f = 100$  Hz) and without seed bubbles assisted at  $G = 377.9 \text{ kg/m}^2 \text{ s}$ .

bubbles are turned on at  $t = 86.5$  s and turned off at  $t = 191$  s. Low frequency seed bubbles not only decrease oscillation amplitudes of pressure drop, outlet fluid temperature and heating surface temperatures, but also shorten oscillation cycle periods of these parameters. Inlet liquid temperatures do not change with and without seed bubbles. Oscillation cycle periods are decreased from 39.8 s to 13.4 s and oscillation amplitudes of pressure drops are decreased from 6.3 kPa to 3.1 kPa by triggering seed bubbles. For the self-sustained flow and heat transfer (no seed bubble data), heating surface temperatures show large amplitude oscillations of more than 15 °C. For instance, the temperature oscillation amplitude at the beginning of heating surface ( $x_{\text{film}} = 0$ ) is 16.5 °C, but it is decreased to 7.5 °C after introduction seed bubbles. Oscillation amplitudes of  $T_{\text{film}}(2.25 \text{ mm}, 0)$  and  $T_{\text{film}}(4.5 \text{ mm}, 0)$  are decreased more than that of  $T_{\text{film}}(0, 0)$ . The standard temperature deviations (Stdev) are also decreased significantly, indicating the improved temperature uniformity of heating surface temperatures after introduction seed bubbles.

As shown in Fig. 6a, seed bubbles are triggered at  $t = t_A$ . Seed bubble guided flow includes two distinct substages in each oscillation cycle: stage B and C, referring to the pressure drop decreased one and increased one, respectively. Flow patterns in the stage B are the alternating liquid and elongated bubble flow, according to the switch frequency identical to the seed bubble frequency  $f$ . For instance, as shown in Fig. 6b, liquid flow is in channel #3 at  $t = 105.1$  s and elongated bubble appears at  $t = 105.17$  s. But the li-

quid flow is repeated at  $t = 105.2$  s (not shown in Fig. 6b). The flow pattern switch frequency is exactly equal to 10 Hz. Evolution of elongated bubble is from the growth of the injected seed bubble. Flow patterns in the stage C are the alternating churn, annular and partial dry-out flow (see Fig. 6b). Fig. 7 shows the sofa shape distribution of heating surface temperatures, identifying the decreased heating surface temperatures and oscillation amplitudes with seed bubble assisted.

#### 4.4. Seed bubbles eliminate flow instabilities at high seed bubble frequencies

High frequency seed bubbles such as  $f > 50$  Hz completely eliminate flow instabilities. An example run is shown in Fig. 8 with operating parameters similar to those in Figs. 6 and 7, but the seed bubble frequency is 1000 Hz. Following the seed bubble triggering time at  $t = 62.4$  s, pressure drop, outlet and inlet fluid temperatures and heating surface temperatures are very stable. The stable pressure drop is 13.5 kPa, approaching the maximum value of the oscillating pressure drop before triggering seed bubbles, indicating that the seed bubble stabilized flow does not increase the pressure drop across the microsystem. Seed bubbles decrease heating surface temperatures of  $T_{\text{film}}(0, 0)$ ,  $T_{\text{film}}(2.25 \text{ mm}, 0)$  and  $T_{\text{film}}(4.5 \text{ mm}, 0)$  by 13–15 °C from their maximum values before triggering seed bubbles, indicating significant heat transfer enhancement. The standard deviation of heating surface temperatures is decreased

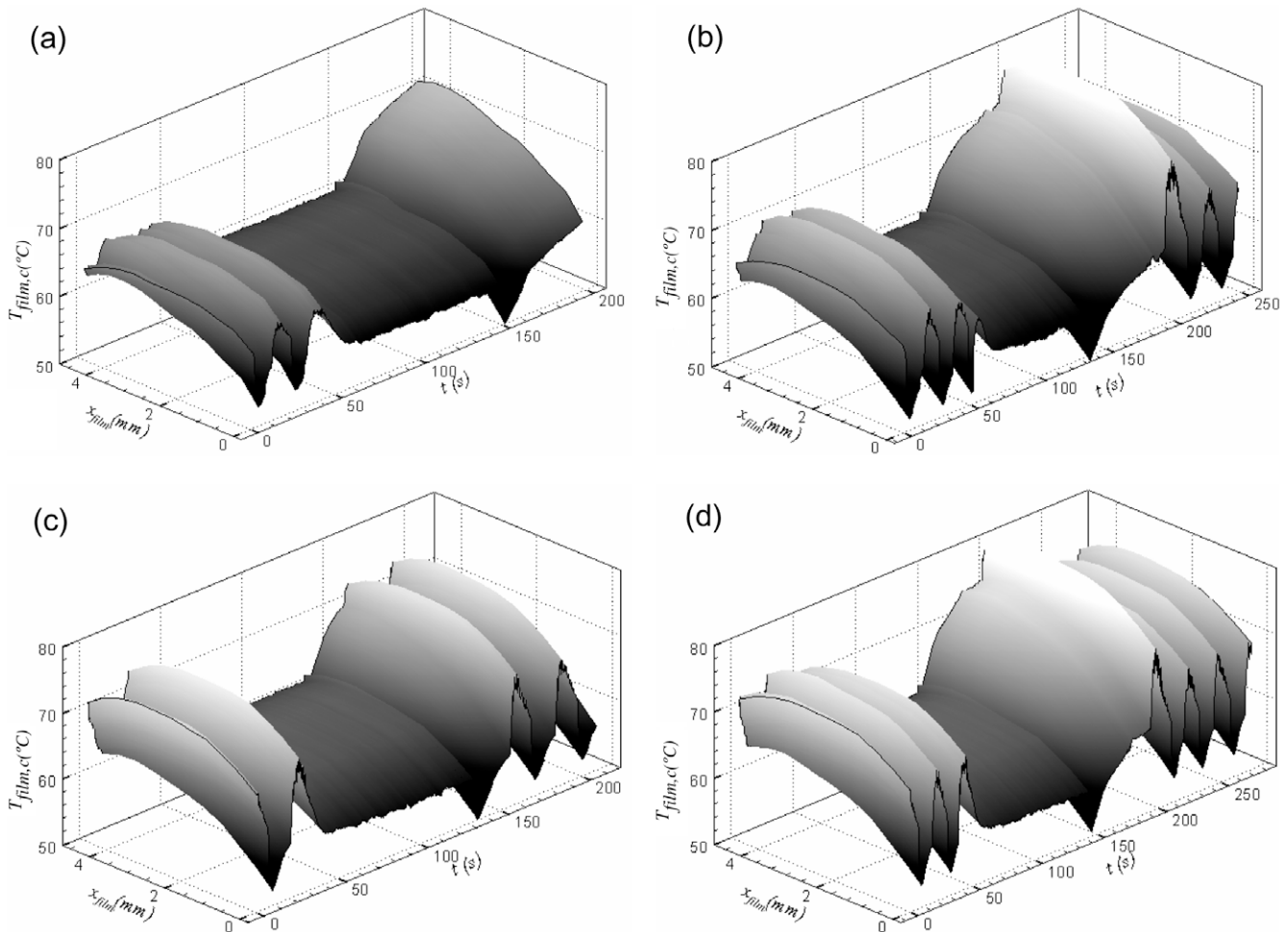


Fig. 12. Effect of boiling numbers on the heating surface temperatures with ( $f = 100$  Hz) and without seed bubbles assisted at  $G = 377.9 \text{ kg/m}^2 \text{ s}$ .

from the maximum value of 4.2 °C without seed bubbles to 2.3 °C with seed bubbles assisted, indicating the improved temperature uniformity by seed bubbles.

The alternating flow in time sequence appeared in the self-sustained oscillation flow or the seed bubble guided flow at  $f = 10 \text{ Hz}$ , does not happen for high seed bubble frequency case. Fig. 8b shows the dynamic flow pattern in channel #3 in the millisecond time-scale. Seed bubble and elongated bubble coexist sequentially in microchannels. In the microchannel upstream such as  $x < 5.3 \text{ mm}$ , seed bubbles are traveling with small growth rate due to the small liquid superheat there. When the seed bubble length is larger than the microchannel hydraulic diameter, elongated bubble appears. The growing elongated bubble may be merged with the downstream one. The seed bubble guided flow ensures a quasi-stable rear interface of elongated bubble which oscillates in a very narrow range of 5.2–5.7 mm. The front interface of elongated bubble is out of the visualization area thus it is not shown in Fig. 8b. Introduction of sufficient seed bubbles in time sequence ensures less opportunity for liquid to reach high superheat, decreasing the thermal non-equilibrium of liquid and vapor phases.

Fig. 9 shows heating surface temperatures at the centerline of  $y_{\text{film}} = 0$ , i.e.,  $T_{\text{film,c}}$ , versus time. The central part gives a stable, low and uniform temperature distribution, behaving a perfect heat transfer performance by seed bubbles.

4.5. Effects of boiling numbers and seed bubble frequencies on the seed bubble guided heat transfer

In this study, the controlling parameters are heat flux, mass flux and seed bubble frequency. The mass flux and heat flux are combined to form the boiling number  $Bo = q/(Gh_{\text{fg}})$ . Fig. 10 shows effect of boiling numbers on pressure drops across the system without seed bubbles and with seed bubbles at  $f = 10 \text{ Hz}$  for runs 27, 32, 37 and 42. Introduction of low frequency seed bubbles shortens oscillation cycle periods and decreases oscillation amplitudes of pressure drops. For instance, Fig. 10a shows that run 27 at  $f = 10 \text{ Hz}$  has the oscillation cycle period of 8.2 s, which is smaller than that of 14.5 s for run 26. The fluctuation amplitude of pressure drop is 4.0 kPa for run 27, which is smaller than that of 7.9 kPa for run 26. Other runs have similar characteristics. The maximum pressure drop during oscillation for the seed bubble guided flow

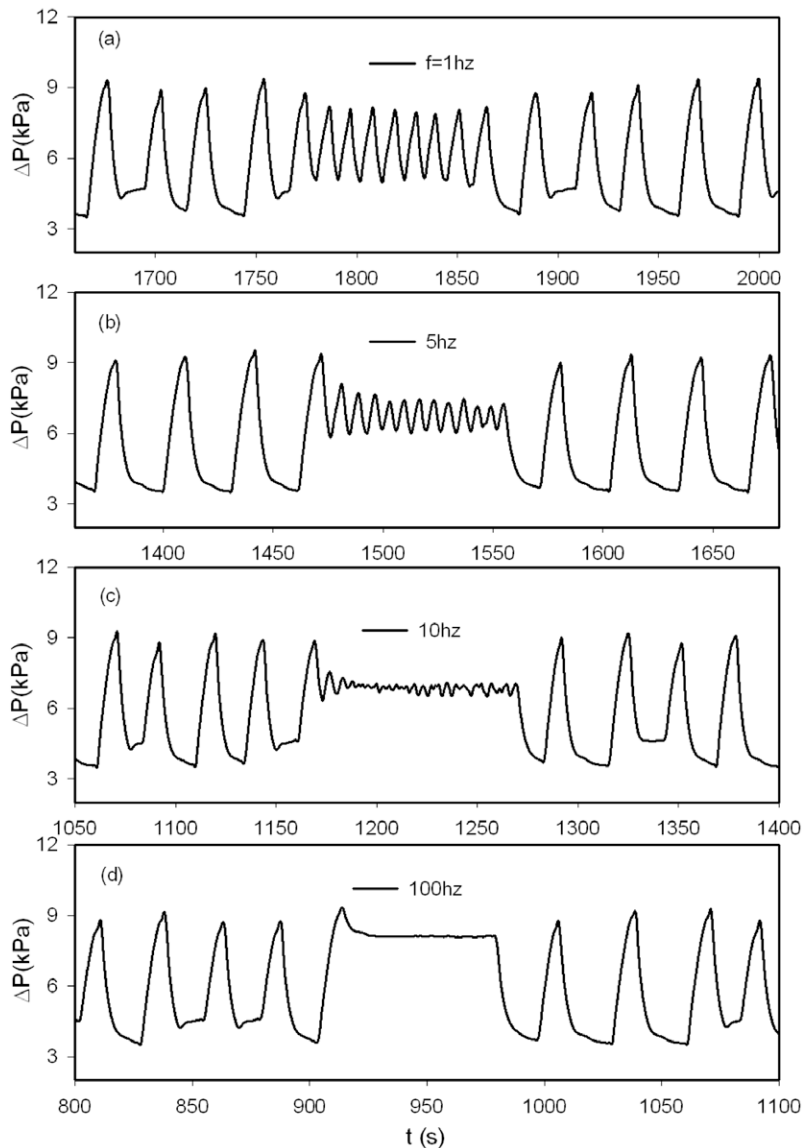


Fig. 13. Effect of seed bubble frequencies on seed bubble guided flow at  $G = 377.9 \text{ kg/m}^2 \text{ s}$ ,  $q = 477.2 \text{ kW/m}^2$ ,  $Bo = 0.002463$ .

at  $f = 10$  Hz is smaller than that for the flow without seed bubbles assisted. The maximum pressure drop is related to bubble growth rate and instantaneous vapor mass qualities in microchannels. Introduction of seed bubbles in time sequence, even at low frequencies, decreases the spatiotemporal liquid superheats. Thus the bubble growth is slowed down, leading to the decreased maximum pressure drop compared to that without seed bubbles. Oscillation cycle periods of pressure drops for the seed bubble guided flow are increased but then decreased with continuous increases in heat fluxes (or boiling numbers), which is similar to those for the oscillation flow without seed bubbles assisted.

Now we consider effect of boiling numbers on the seed bubble guided flow at high seed bubble frequency of 100 Hz. Fig. 11 had the mass flux of  $377.9 \text{ kg/m}^2 \text{ s}$ . Completely stable pressure drops are identified for the seed bubble guided flow with continuous increases in heat fluxes, or boiling numbers. The stable pressure drops for the seed bubble guided flow are almost the same as the maximum values for the flow without seed bubbles. Fig. 12 shows the decreased and uniform heating surface temperatures (see the central part) with running parameters identical to those in Fig. 11.

Seed bubble frequency is an important parameter to influence the seed bubble guided flow. The transition seed bubble frequency from oscillation to stable flow depends on mass flux and heat flux, which are combined to form the boiling number. In this study, completely stable flow appears when the seed bubble frequency is larger than several tens Hertz. Fig. 13 shows pressure drops versus time for mass flux of  $377.9 \text{ kg/m}^2 \text{ s}$  and heat flux of  $477.2 \text{ kW/m}^2$  at seed bubble frequencies of 1, 5, 10 and 100 Hz, respectively. The boiling flow is influenced by seed bubbles apparently even at very low seed bubble frequencies such as  $f = 1$  and 5 Hz. Seed bubbles significantly narrow oscillation amplitudes of pressure drops at low seed bubble frequencies. Oscillation amplitudes become very small at  $f = 10$  Hz. Completely stable flow appears at  $f = 100$  Hz.

Even though the spatiotemporal temperatures of vapor and liquid phases in microchannels are not measured directly, we conclude that the thermal non-equilibrium of the two phases is decreased with increases in seed bubble frequencies. The following description supports this conclusion. In this study, the length of the heating surface area is shorter than the microchannel. Thermal conduction of the silicon substrate heats the channel wall surface to reach the fluid saturation temperature at the upstream of the heating area for some runs. As shown in Fig. 14a, vapor phase can reach the microheater area during the vapor production stage

in a cycle for the no seed bubble case. Fig. 14b–e shows that locations where seed bubbles have apparent growth are moved to the microchannel downstream with continuous increases in seed bubble frequencies, inferring the decreased liquid temperatures with increases in seed bubble frequencies. This is true because seed bubbles have the size of several microns, the seed bubble growth in microchannels is heat transfer controlled.

We consider effect of seed bubble frequencies on the heating surface temperatures in Fig. 15. Temperatures at the centerline of  $y_{\text{film}} = 0$ , i.e.,  $T_{\text{film,c}}$  are plotted versus the attached axial coordinate of  $x_{\text{film}}$ . The four subfigures refer to the boiling numbers of  $2.263 \times 10^{-3}$ ,  $2.495 \times 10^{-3}$ ,  $2.040 \times 10^{-3}$  and  $2.359 \times 10^{-3}$ . In each subfigure of Fig. 15, the boiling heat transfer without seed bubbles assisted and the seed bubble guided heat transfer at  $f = 10$  Hz display oscillation behavior. Temperatures are given for both the maximum and minimum values within their fluctuations. For instance, the two black curves represent the maximum and minimum limits of the oscillation temperatures for the no seed bubble data. Meanwhile, the two red curves show the maximum and minimum limits of the oscillation temperatures at the seed bubble frequency of 10 Hz. The seed bubble guided heat transfer at  $f = 100$ , 1000 and 2000 Hz is stable thus only one curve is given for each seed bubble frequency. It is observed that the low seed bubble frequency of 10 Hz narrows the temperature fluctuation range and decreases the heating surface temperatures. The higher the seed bubble frequency, the more decreased heating surface temperatures are. For most runs, heating surface temperatures are decreased by more than  $10^\circ\text{C}$  at the seed bubble frequencies of 1000 or 2000 Hz. If boiling numbers are relatively low such as shown in Fig. 15a and b, the seed bubble guided heat transfer can maintain heating surface temperatures to be higher than the fluid saturation temperature by several degrees, note that the saturation temperature of acetone is  $56.3^\circ\text{C}$  at atmospheric pressure. Besides, when the seed bubble frequency attains 1000 Hz, further increase in seed bubble frequencies will no longer decrease the heating surface temperatures. Thus the seed bubble frequency of 1000–2000 Hz is named as the saturation frequency, at which complete thermal equilibrium of vapor and liquid phases can be reached in microchannels. The saturation seed bubble frequency may be different for different microsystem design, working fluids and running parameters.

Spatial-averaged heat transfer coefficients are calculated based on Eq. (4) and are shown in Table 4 for the boiling flow with and without seed bubbles, corresponding to the four boiling numbers

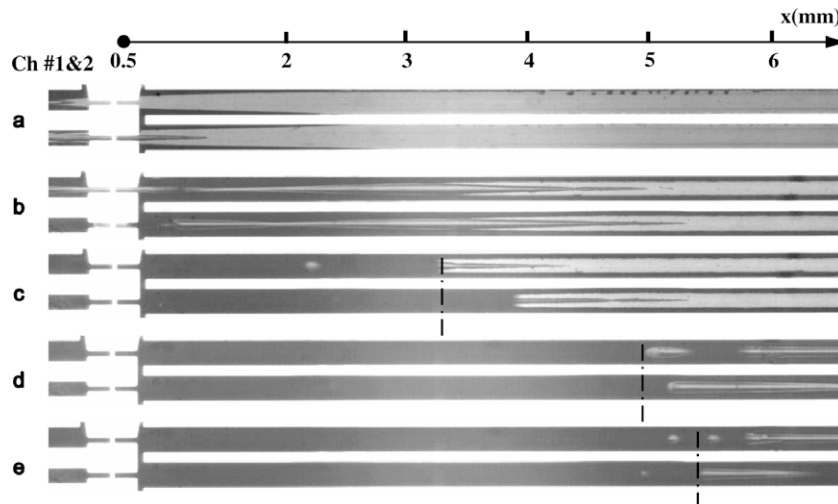
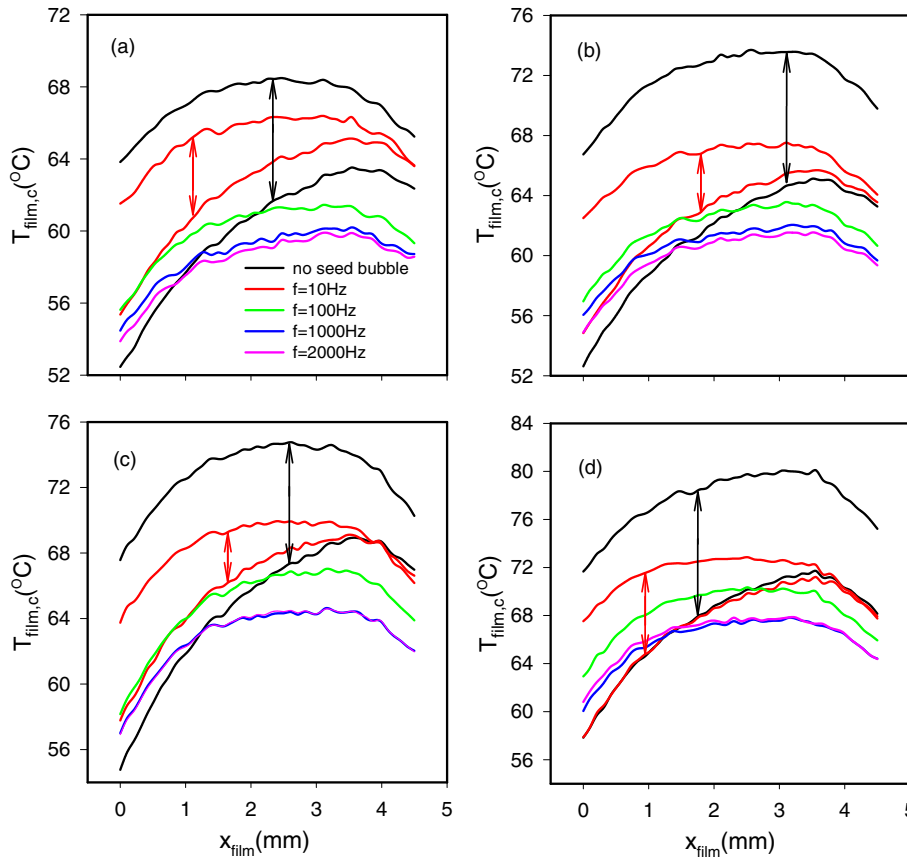


Fig. 14. Effect of seed bubble frequencies on flow patterns in the microchannel upstream. (a) No seed bubble, (b)  $f = 10$  Hz, (c)  $f = 100$  Hz, (d)  $f = 1000$  Hz, (e)  $f = 2000$  Hz, the operating parameters are  $G = 377.94 \text{ kg/m}^2 \text{ s}$ ,  $q = 452.82 \text{ kW/m}^2$ ,  $Bo = 0.00234$ .



**Fig. 15.** Decreased heating surface temperatures of seed bubble guided heat transfer. (a)  $G = 377.9 \text{ kg/m}^2 \text{ s}$ ,  $q = 439.6 \text{ kW/m}^2$ ,  $Bo = 0.002263$ . (b)  $G = 377.9 \text{ kg/m}^2 \text{ s}$ ,  $q = 483.9 \text{ kW/m}^2$ ,  $Bo = 0.002495$ . (c)  $G = 598.4 \text{ kg/m}^2 \text{ s}$ ,  $q = 625.4 \text{ kW/m}^2$ ,  $Bo = 0.002040$ . (d)  $G = 598.4 \text{ kg/m}^2 \text{ s}$ ,  $q = 723.4 \text{ kW/m}^2$ ,  $Bo = 0.002359$ .

**Table 4**  
Heat transfer coefficients with and without seed bubbles.

$G \text{ (kg/m}^2\text{s)}$	$q \text{ (kW/m}^2\text{)}$	$Bo \times 10^3$	No seed bubble		10 Hz		100 Hz	1000 Hz	2000 Hz
			$\alpha_{\min} \text{ (kW/m}^2\text{K)}$	$\alpha_{\max} \text{ (kW/m}^2\text{K)}$	$\alpha_{\min} \text{ (kW/m}^2\text{K)}$	$\alpha_{\max} \text{ (kW/m}^2\text{K)}$	$\alpha \text{ (kW/m}^2\text{K)}$	$\alpha \text{ (kW/m}^2\text{K)}$	$\alpha \text{ (kW/m}^2\text{K)}$
377.9	439.60	2.263	24.30	67.87	29.83	43.49	69.91	108.11	129.47
	483.90	2.495	18.68	56.75	29.56	45.73	52.07	68.08	78.30
598.4	625.40	2.040	22.62	43.86	30.84	38.53	43.50	56.64	56.61
	723.40	2.359	20.30	38.44	28.86	39.14	35.66	44.78	43.58

shown in Fig. 15. Because the no seed bubble run and seed bubble run at  $f = 10 \text{ Hz}$  display fluctuation behavior, heat transfer coefficients are given for the minimum and maximum values, corresponding to the maximum and minimum heating surface temperatures. The seed bubble runs at  $f = 100, 1000$  and  $2000 \text{ Hz}$  are absolutely stable, thus there is only one heat transfer coefficient in Table 4. Significant heat transfer enhancement is observed by seed bubbles. For example, heat transfer coefficients are varied from 18.68 to 56.75  $\text{kW/m}^2\text{K}$  for the no seed bubble data at the boiling number of  $2.495 \times 10^{-3}$ , but they are 52.07, 68.08 and 78.30  $\text{kW/m}^2\text{K}$  with seed bubbles assisted at  $f = 100, 1000$  and  $2000 \text{ Hz}$ , which are several times higher than the minimum value for the no seed bubble data.

4.6. Comparison with other studies

In macroscale boiling systems for power and chemical engineering applications, liquid–vapor two-phase flow instabilities have been studied widely. In such systems the thermal equilibrium

of liquid and vapor phases can be easily reached due to the roughed channel wall surface. Two-phase flow instabilities are caused either by the compressible volume for pressure drop type instability, or by the two-phase density wave transportation in the system for density wave oscillation. However, if a system is made by microfabrication technique and the hydraulic diameter is down to micron meter, bubble nucleation needs high liquid and wall superheats. Flow instability in micro-boiling systems is caused by the rapid bubble growth and the flow reversal in channels. To the authors’ knowledge, there are three ways to mitigate flow instabilities in microchannels. The first means is to set an inlet fluid restriction at the upstream of microchannels. This method, however, is well used in macrosystems to suppress the pressure drop type instability. The mitigation mechanism of this method is to suppress the flow reversal of vapor phase in microchannels. Definitely it needs larger pressure drop across the microsystems than that without the inlet fluid restrictions. A recent study by Wang et al. (2008) belongs to this method. A similar method is to use diverging cross-section microchannels in stead of straight

ones, such as reported by Lee and Pan (2008). The second method is to use fabricated nucleation sites on the microchannel wall surface. The flow instability mitigation mechanism is to decrease wall superheats to trigger the boiling heat transfer in microchannels, as reported by Kuo and Peles (2008). The third method is to use a hybrid technique combining fabricated nucleation sites and inlet pressure drop elements to suppress flow instabilities in microchannels. As noted by Kandlikar et al. (2006), wall superheats are generally high, even in the presence of right sized artificial cavities on the wall surface. Introduction of artificial cavities alone may not be enough to completely suppress the flow instabilities. In such cases, introduction of pressure drop elements at the upstream of microchannels is expected to reduce the flow reversal.

We proposed the seed bubble technique to suppress the two-phase flow instabilities. This method is thoroughly different from those described above. It almost does not increase the pressure drop across microsystems, in the present data range. Benefits of this method are the stabilization of flow and heat transfer, improvement of the uniformity of heating surface temperatures and heat transfer enhancement. The seed bubble technique is an active control of the boiling heat transfer system. Flow and heat transfer performance can be easily changed by altering the seed bubble frequencies. Heating surface temperatures can be controlled by changing the seed bubble frequencies alone, without change to the flow rate.

## 5. Conclusions

Seed bubbles are created on microheaters at the microchannel upstream and driven by a pulse voltage signal. The seed bubble technique was proposed by the authors here recently to improve the flow and heat transfer characteristics in microchannels. For the forced convection flow, when heat flux at the wall surface is continuously increased, flow instability is self-sustained in microchannels with large amplitudes and long periods. Introduction of low frequency ( $\sim 10$  Hz) seed bubbles not only decreases oscillation amplitudes of pressure drops, fluid inlet and outlet temperatures and heating surface temperatures, but also shortens oscillation cycle periods. High frequency ( $\sim 100$  Hz or high) seed bubbles completely suppress the flow instability and the heat transfer system behaves stable pressure drops, fluid inlet and outlet temperatures and heating surface temperatures. Quasi-stable spheric bubble and elongated bubble are the major flow patterns in microchannels at high seed bubble frequency such as  $f > 100$  Hz. Pressure drop for the seed bubble guided flow is either smaller than or almost the same as the maximum pressure drop during the oscillation flow without seed bubbles assisted. Heating surface temperatures are continuously decreased with increases in seed bubble frequencies. A saturation seed bubble frequency of 1000–2000 Hz can be reached, at which heat transfer enhancement attains the maximum degree, inferring a complete thermal equilibrium of vapor and liquid phases in microchannels. Benefits

of the seed bubble technique are the stabilization of flow and heat transfer, decreasing heating surface temperatures, and improving temperature uniformity of the heating surface.

## Acknowledgements

This work is supported by the National Science Fund for Distinguished Young Scholars from the National Natural Science Foundation of China (No. 50825603).

In this paper we use the seed bubble concept to improve flow and heat transfer in microchannels. The similar idea happens to be already covered in Thome and Dupont (2007). The authors appreciate Prof. Thome's great idea on bubble generators for heat transfer.

## References

- Chang, K.H., Pan, C., 2007. Two-phase flow instability for boiling in a microchannel heat sink. *Int. J. Heat Mass Transfer* 50, 2078–2088.
- Hetsroni, G., Mosyak, A., Pogrebnik, E., Segal, Z., 2006. Periodic boiling in parallel microchannels at low vapor quality. *Int. J. Multiphase Flow* 32, 1141–1159.
- Huh, C., Kim, J., Kim, M.H., 2007. Flow pattern transition instability during flow boiling in a single microchannel. *Int. J. Heat Mass Transfer* 50, 1049–1060.
- Kandlikar, S.G., Kuan, W.K., Willistein, D.A., Borrelli, J., 2006. Stabilization of flow boiling in microchannels using pressure drop elements and fabricated nucleation sites. *J. Heat Transfer ASME* 128, 389–396.
- Kuo, C.J., Peles, Y., 2008. Flow boiling instabilities in microchannels and means for mitigation by reentrant cavities. *J. Heat Transfer ASME* 130, 1–10.
- Lee, P.C., Pan, C., 2008. Boiling heat transfer and two-phase flow of water in a single shallow microchannel with a uniform and diverging cross section. *J. Micromech. Microeng.* 18 (025005), 13 pp.
- Li, J., Cheng, P., 2004. Bubble cavitation in a microchannel. *Int. J. Heat Mass Transfer* 47, 2689–2698.
- Lin, L., 1998. Microscale thermal bubble formation, thermophysical phenomenon and applications. *Microscale Thermophys. Eng.* 2, 71–85.
- Muwanga, R., Hassan, I., MacDonald, R., 2007. Characteristics of flow boiling oscillations in silicon microchannel heat sinks. *J. Heat Transfer ASME* 129, 1341–1351.
- Qu, W.L., Mudawar, I., 2004. Transport phenomena in two-phase microchannel heat sinks. *J. Electronic Packaging ASME* 126, 213–224.
- Takahashi, K., Weng, J.G., Tien, C.L., 1999. Marangoni effect in microbubble systems. *Microscale Thermophys. Eng.* 3, 169–182.
- Thome, J.R., 2006. State-of-the-art overview of boiling and two-phase flows in microchannels. *Heat Transfer Eng.* 27 (9), 4–19.
- Thome J.R., Dupont V., 2007. Heat transfer assembly, European Patent EP 1779052 B1, November 28, 2007.
- Tadrist, L., 2007. Review on two-phase flow instabilities in narrow spaces. *Int. J. Heat Fluid Flow* 28, 54–62.
- Wang, G.D., Cheng, P., Bergles, A.E., 2008. Effects of inlet/outlet configuration on flow boiling instability in parallel microchannels. *Int. J. Heat Mass Transfer* 51, 2267–2281.
- Wu, H.Y., Cheng, P., 2004. Boiling instability in parallel microchannels at different heat flux. *Int. J. Heat Mass Transfer* 47 (17–18), 3631–3641.
- Wu, H.Y., Cheng, P., Wang, H., 2006. Pressure drop and flow boiling instabilities in silicon microchannel heat sinks. *J. Micromech. Microeng.* 18, 2138–2146.
- Xu, J.L., Zhou, J.J., Gan, Y.H., 2005a. Static and dynamic flow instability of a parallel microchannel heat sink at high heat fluxes. *Energy Conversion Manag.* 46 (2), 313–334.
- Xu, J.L., Gan, Y.H., Zhang, D.C., Li, X.H., 2005b. Microscale boiling heat transfer in a micro-timescale at high heat fluxes. *J. Micromech. Microeng.* 15, 362–376.
- Yaws, C.L., 1999. *Chemical Properties Handbook*. McGraw-Hill, New York.